Dislocation Generation in Experimentally Shocked Olivine Crystals

Jacob A. Tielke, Anne H. Peslier, Roy Christoffersen, Timmons M. Erickson, Christopher J. Cline, Ryan S. Jakubek, Mark J. Cintala, Zia Rahman, Marc D. Fries, Pierre Bouilhol

JGR Planets

RESEARCH ARTICLE
10.1029/2021JE007042

Key Points:

- Olivine crystals were experimentally shocked to produce dislocations
- Dislocation densities are sensitive to crystallographic orientation with respect to shock wave propagation
- Dislocations cause the peak width in Raman spectra to increase with increasing shock pressure

Supporting Information:

Supporting Information may be found in the online version of this article.

Correspondence to:

J. A. Tielke,
jtielke@ldeo.columbia.edu

Citation:

Tielke, J. A., Peslier, A. H., Christoffersen, R., Erickson, T. M., Cline II, C. J., Jakubek, R. S., et al. (2022). Dislocation generation in experimentally shocked olivine crystals. *Journal of Geophysical Research: Planets*, *127*, e2021JE007042. https://doi.org/10.1029/2021JE007042

Received 23 AUG 2021
Accepted 21 MAY 2022

Author Contributions:

Conceptualization: Anne H. Peslier
Funding acquisition: Anne H. Peslier
Investigation: Jacob A. Tielke, Anne H. Peslier
Methodology: Jacob A. Tielke, Anne H. Peslier
Project Administration: Anne H. Peslier
Resources: Anne H. Peslier
Supervision: Anne H. Peslier
Writing – review & editing: Jacob A. Tielke, Anne H. Peslier

Dislocation Generation in Experimentally Shocked Olivine Crystals

Jacob A. Tielke[1,2], Anne H. Peslier[3], Roy Christoffersen[3], Timmons M. Erickson[3], Christopher J. Cline II[3], Ryan S. Jakubek[3], Mark J. Cintala[4], Zia Rahman[3], Marc D. Fries[4], and Pierre Bouilhol[5]

[1]Lamont-Doherty Earth Observatory, Columbia University, Palisades, NY, USA, [2]Lunar and Planetary Institute, Universities Space Research Association, Houston, TX, USA, [3]Jacobs, Mail Code XI3, Astromaterials Research and Exploration Science, NASA-Johnson Space Center, Houston, TX, USA, [4]Astromaterials Research and Exploration Science, NASA-Johnson Space Center, Houston, TX, USA, [5]Université de Lorraine, Centre de Recherches Pétrographiques et Géochimiques CNRS, Nancy, France

Abstract During shock metamorphism, crystals in planetary bodies are exposed to extreme conditions of stress, pressure, and temperature, resulting in the development of a range of shock-induced defects, including dislocations. To investigate the shock-induced development of dislocations in olivine, one of the most common minerals found in meteorites and other planetary samples, a series of shock experiments were carried out on olivine single crystals. Olivine crystals were shocked to peak reverberation pressures ranging from 21.3 to 58.7 GPa in a flat-plate accelerator. The crystals were characterized using electron backscatter diffraction (EBSD), Raman spectroscopy, transmission electron microscopy (TEM), Fourier transform infrared spectroscopy, and electron microprobe. EBSD analyses reveal that geometrically necessary dislocations form on all common slip systems. Raman spectroscopy reveals that the full width at half height of characteristic peaks increases linearly as a function of shock pressure. Dislocation loops with the Burgers vector b = [001] have higher densities near fractures as revealed by TEM analyses, whereas dislocations away from fractures are more dependent on the crystal orientation relative to impact direction. The type and density of dislocations that form during shock are largely independent of the starting hydrogen content of crystals. Calculations that incorporate post-shock cooling rates of meteorites ejected from planetary surfaces, dislocation annihilation rates in olivine, and dislocation densities measured in shocked olivine suggest that shock-induced dislocations are preserved in olivine in meteorites ejected from planetary bodies and therefore give insight into the conditions of ancient impact events in the solar system.

Plain Language Summary Most of the crystals in the solar system, including those found on the moon, mars, and asteroids, have been subject to impact events, which send shock waves through the rocks and produce extreme conditions of temperature, pressure, and stress. These shock events may change the physical and chemical properties of the rocks and introduce defects in their crystal structure. We performed a series of experiments to understand how dislocations, which are line defects in crystals, form during shock. We found that the density of dislocations estimated using electron microscopy and the width of peaks in Raman spectra both increase with increasing shock in laboratory experiments. These results may be used to gain insight into the nature of past shock and impact events that occurred in our solar system.

1. Introduction

1.1. Shock-Induced Defects

Shock waves that are generated during impact events result in changes in the physical and chemical properties of planetary materials (Sharp & DeCarli, 2006). Depending on the conditions of shock and the composition of the target rocks, shock may result in partial melting, amorphization, the development of high-pressure polymorphs, fracturing, and increases in the density of dislocations (i.e., line defects) in crystals (Fritz et al., 2017; Leroux, 2001; Stöffler et al., 1991, 2018). These dislocations act as a short-circuit diffusive pathway, which result in the evolution of the chemical properties of minerals (Piazolo et al., 2016).

The importance of the degree of shock in the evolution of planetary materials has motivated the search for scaling relationships (i.e., barometers or piezometers) that relate the degree of shock to the deformation features in the shocked material. To date, some of the most reliable markers of shock have been the presence of high-pressure polymorphs of minerals (Binns, 1970; Cavosie et al., 2018; Chao et al., 1960; Erickson et al., 2017; Glass & Fries, 2008; Greshake et al., 2013; Hu & Sharp, 2017; Malavergne et al., 2001; Shen et al., 2001; Tomioka & Miyahara, 2017; Tschauner et al., 2020; Xie et al., 2002; 2006), mechanically twinned crystals of zircon and quartz (Erickson et al., 2016; Goltrant et al., 1991), and the presence of maskelynite (Fritz et al., 2019; Gibbons & Ahrens, 1977; Jaret et al., 2015; Rubin, 2015) and of shock melt (Walton & Herd, 2007; Walton & Shaw, 2009). The dependence of the density of discrete arrays of defects, referred to as planar deformation features, also varies systematically as a function of shock pressure (Takenouchi et al., 2019). Shock-induced lattice strain has also been investigated using X-ray diffraction analyses of experimentally shocked (Uchizono et al., 1999) and Martian (Jenkins et al., 2019) olivine crystals. Previous work has investigated the relationship between fracture density and orientation to the degree of shock in olivine. Fracture density increases nearly linearly with shock pressure <20 GPa for olivine-rich rocks, and at >20 GPa is either being insensitive to shock pressure or decreasing with increasing shock pressure (Bauer, 1979). Fracture orientation was observed to be independent of peak shock pressure (Reimold & Stöffler, 1978).

1.2. Why Study Olivine?

Olivine is one of the most common minerals in the solar system; it is present in meteorites that originated from asteroids (Ashworth & Barber, 1975; Brearley et al., 1998; Mittlefehldt et al., 2018) Mars (Fritz et al., 2005; Greshake et al., 2004; McSween, 2015; Peslier et al., 2010; Udry et al., 2020), and the Moon. Olivine crystals are also common in rocks sampled by astronauts on the Moon surface during the Apollo missions (Rhodes & Hubbard, 1973). One of the most characteristic features of shocked olivine is the high density of lattice dislocations (Bauer, 1979; Carter et al., 1968; Reimold & Stöffler, 1978). Dislocations are important in both facilitating deformation and recording past deformations events, and even though a shock event can cause a temperature increase, dislocations in olivine are relatively likely to be preserved due to that mineral's high melting temperature (generally >1500°C, depending on iron content; e.g., Ohtani and Kumazawa (1981)). Therefore, deformation features will be recorded as it will remain crystalline at high shock pressures and therefore may provide information about a relatively large range of shock conditions.

1.3. Controls on Dislocation Activity

An extensive literature exists describing the controls of the physical and chemical environment on the relative activities of different olivine slip systems under controlled laboratory conditions. The velocity of dislocations in olivine is controlled by stress (Durham & Goetze, 1977), temperature (Demouchy et al., 2009, Demouchy et al., 2013; Evans & Goetze, 1979; Hansen et al., 2019; Mei et al., 2010), pressure (Dixon & Durham, 2018; Raterron et al., 2011), hydrogen content (colloquially called “water” in some of the literature; Chopra & Paterson, 1984; Mackwell et al., 1985; Mei & Kohlstedt, 2000; Tielke et al., 2019; Wallis et al., 2019), oxygen fugacity (Bai et al., 1991; Keefner et al., 2011), and silica activity (Bai et al., 1991; Tielke et al., 2017). In contrast, the density of dislocations is controlled primarily by the orientation of crystals with respect to an applied stress (Bai & Kohlstedt, 1992). Therefore, observations of both the types and densities of dislocations that form during shock have the potential to yield valuable information about the conditions of shock in planetary materials. These observations highlight the need for scaling relationships that relate orientation-dependent microstructural observations to peak shock pressure in minerals common in planetary samples.

In particular, the influence of the orientation of shock wave propagation with respect to crystallographic orientations has yet to be investigated. Raman is a promising method to address this issue because the peak positions in Raman spectra have been proposed to shift systematically with increasing shock pressure in olivine (Miyamoto & Ohsumi, 1995) and the full width half height (FWHH) of characteristic peaks in Raman spectra have been observed to increase with shock pressure in experimentally shocked olivine (Farrell-Turner et al., 2005; Shinno et al., 1999).

1.4. Observation of Dislocations

Once shock waves that generate pressures exceeding the Hugoniot elastic limit (HEL) have propagated through a material, dislocations that were created and preserved (i.e., not annihilated during post-shock thermal increases) in the lattices of shocked minerals may be observed using a variety of techniques. The oxidation-decoration technique (Kohlstedt et al., 1976) may be used to observe the cores of dislocations in iron-bearing olivine using either transmitted light or scanning electron microscopy. Micro-Raman spectroscopy has been used to image local strain around edge dislocations in deformed materials (Irmer & Jurisch, 2007; Kokubo et al., 2018). Transmission electron microscopy (TEM) provides the highest resolution images of dislocations and allows for determination of the burgers vector of dislocations (Leroux et al., 1994). The Burgers vector represents the direction and amount of distortion generated by the lattice dislocations. Data from electron backscatter diffraction (EBSD) may also be processed to determine the density and types of geometrically necessary dislocations (GNDs; meaning dislocations required to explain observed orientation gradients in the crystal lattice) present in deformed materials (e.g., Hielscher et al., 2019; Wheeler et al., 2009; Wallis et al., 2016). In this study, we report results from a series of shock experiments on olivine crystals to investigate the influence of shock pressure, crystallographic orientation, and hydrogen content on the generation of dislocations as determined from EBSD, Raman, and TEM data.

2. Methods

Two crystals (labeled K1 and K2) originating from Kohistan, Pakistan (Bouilhol et al., 2012), were chosen for the experiments based on their large size (>1 cm^3) and high hydrogen content (>60 ppm weight H_2O). This enabled multiple experiments to be performed on each crystal, thus minimizing compositional changes between experiments. All sample preparation, experiments, and analyses were carried out at the Astromaterials Research and Exploration Science division at NASA's Johnson Space Center. Olivine single crystals were adhered to glass slides using acetone-soluble mounting adhesive (Crystalbond 509 sticks), made into cylinders using a diamond coring drill, and then sliced into discs 6.3 mm in diameter and 0.8 mm thick using a diamond saw. Crystals used in experiments FPA-3811, FPA-3812, FPA-3813, and FPA-3814 were oriented such that the direction of shock wave propagation was parallel to the [010] crystallographic direction, an orientation referred to here as the $[010]_c$ orientation. Crystals used in experiments FPA-3816, FPA-3817, and FPA-3818 were oriented such that the direction of shock wave propagation was at 45° to both the [100] and [010] crystallographic directions, which are referred to here as the $[110]_c$ orientation. The subscript "c" refers to the orientation of maximum compression for a fictitious cubic lattice for both orientations (e.g., Durham & Goetze, 1977). Some of the olivine discs were dehydrated prior to shock to test whether the development of microstructures is dependent upon the hydrogen content of the crystals. This was done by annealing the crystals at 1300°C for 24 hr in a 1-atm gas-mixing furnace using a mixture of CO-CO_2 to maintain an oxygen fugacity at the fayalite-magnetite-quartz buffer. All experiments were carried out on single crystal discs, except for FPA-3817 and FPA-3818, which were half discs of natural and annealed olivine placed adjacent to each other inside the same capsule. For the case of experiments containing two half discs, data from natural crystals are referred to as 3817a and 3818a, whereas annealed crystals are referred to as 3817b and 3818b. Experiments FPA-3817 and FPA-3818 were designed as diffusion couple experiments, consisting of a half disc of dehydrated olivine placed adjacent to a half disc natural olivine, thus providing a chemical potential gradient to move hydrogen from the natural olivine into the dehydrated olivine during shock.

The olivine discs and target assemblies were cleaned using a series of ultrasonic baths to ensure that the samples were not contaminated with hydrogen from atmospheric sources or from fluids used during preparation. The discs were placed in an ultrasonic bath of acetone for 30 min and then placed in an ultrasonic bath of isopropanol for 30 min. Different cleaning procedures were used for the metal target assemblies that encapsulated the crystals during impact experiments. For FPA-3811 and FPA-3812, the target assembly was placed in an ultrasonic bath of degreaser for 60 min. FPA-3813 and FPA-3814 were placed in an ultrasonic bath of degreaser for 60 min, acetone for 30 min, and isopropanol for 30 min. For FPA-3816, FPA-3817, and FPA-3818, the assemblies were scrubbed with an iron brush using degreasing agent, rinsed with water, then placed in an ultrasonic bath of mineral spirits for 1 min, degreaser for 30 min, acetone for 30 min, and isopropanol for 30 min. In all cases, the cleaned olivine discs and target assemblies were placed in an oven at a temperature of 75°C and a vacuum condition of 0.004 MPa for at least 12 hr before being moved into the flat plate accelerator (FPA) chamber immediately before each experiment. An additional heating step was used by placing a heating element with a J-type thermocouple

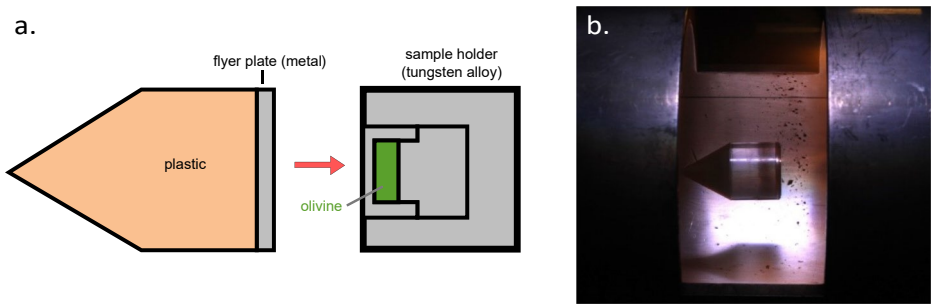

Figure 1. (a) Illustration (not to scale) of assemblies used in flat plate accelerator experiments. The projectile is propelled from the left and impacts the sample holder on the right. (b) One of two photographs of a projectile in flight (FPA-3811), traveling from left to right at 0.85 km s^{-1}. The sample in its holder is out of the field of view, just inside the edge of the pipe to the right. The tilt of the flyer plate, visible on the flat side of the projectile, is less than 0.9°.

around the target assembly for FPA-3812. In that assembly, the temperature was maintained between 80°C and 99°C under vacuum conditions for 2 hours prior to impact. The heating element and thermocouple were destroyed upon impact, and no measurable differences compared to the other experiments were observed so this procedure was not used in the rest of the experiments.

The olivine discs were shocked under vacuum conditions (200 mTorr) in tungsten alloy (Fansteel) capsules at peak pressures ranging from 21.3 to 58.7 GPa in a FPA (Figure 1) at the Experimental Impact Laboratory at NASA's Johnson Space Center. The range of peak shock pressures was chosen to include the range of conditions experienced by most planetary materials (Stöffler et al., 1991). The FPA is a single-stage powder gun built around a barrel with a 25-mm bore through which projectiles are propelled with gunpowder. Peak shock pressures were achieved by impacting flyer plates of known density and traveling at known velocities with the target assembly described by Gibbons and Ahrens (1971). The desired shock level is generated by the impact of a metallic flyer plate into a metal sample-holder assembly, both with known equations of state, at a speed determined through an algebraic solution of a one-dimensional impedance-matching condition (Duvall & Fowles, 1963; Gault, 1963). A reverberation technique is used to raise the pressure felt by the sample to levels higher than those possible by single shocks at these scales (Gibbons, 1974; Gibbons & Ahrens, 1971; Hörz, 1970). The largest pressure achieved during an experiment using this technique is referred to as the peak shock pressure. This process results in a smaller change in shock-induced entropy and, therefore, post-shock temperature, than would occur had the stress increase occurred via a single shock of the same amplitude. Therefore, the shock-induced defects generated by this technique can be more readily observed compared to single shock events as subsequent post-shock annealing has a smaller influence on defect concentrations.

The velocity of the flyer plate was calculated by measuring the timing of interruptions between a series of three lasers during free flight of the projectile. Two Nikon D40x digital cameras, mounted orthogonally, photograph the projectile just a few centimeters before impact under illumination from an electronically triggered high-speed (under 250 ns) flash unit (Figure 1b). The two resulting photographs are used to calculate the three-dimensional orientation of the flyer plate. Inclination of the flyer plate was <2° for all experiments used in this study.

Each target assembly, containing a shocked olivine crystal or diffusion couple, was removed from the vacuum chamber immediately after impact and carefully turned down on a lathe. The thin layer of remaining fansteel was then removed to expose the sample. Each sample was subsequently mounted in epoxy and polished using a series of either alumina or diamond lapping film down to a particle size of 3 μm. The sample was then polished using 1 μm diamond paste on a Minimet polisher for 60 min. Lastly, the sample was polished in a colloidal silica solution on a Buehler Vibromet polisher for 60 min. The samples were cleaned using isopropanol and dried before depositing 8 nm of carbon onto the polished surface for EBSD analyses.

2.1. Fourier Transform Infrared Spectroscopy

A Hyperion 3000 microscope of a Bruker Vertex 70 Fourier transform infrared spectroscopy (FTIR) was used to quantify the presence of hydrogen in the starting crystals. Samples were prepared for FTIR by polishing both sides of unshocked olivine discs down to 3 μm alumina grit. The samples were cleaned by submersion in

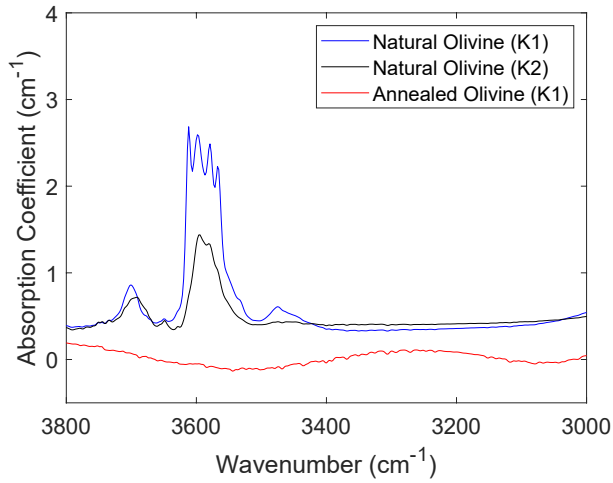

Figure 2. Unpolarized absorbance Fourier transform infrared spectroscopy spectra in the O-H region for natural olivine K1 (blue), K2 (black), and the dehydrated olivine, that is, annealed at 1300°C for 24 hr at 1 atm with oxygen fugacity controlled at the fayalite-magnetite-quartz conditions (red). Bands at 3,710 cm^{-1} are indicative of the presence of serpentine, likely as inclusions invisible even under high magnification microscope (60×). Bands near 3,600 cm^{-1} characterize H incorporated in the olivine structure. Spectra are normalized to 1 cm thickness.

acetone and then submersion in isopropanol and placed in a drying oven at 80°C for at least 1 hr prior to obtaining measurements. Spectra were collected from an average of 128 scans at a resolution of 4 cm^{-1} with an unpolarized beam operating in transmission mode. Hydrogen contents were calculated using the calibration of Paterson (1982) multiplied by a factor of 3.5 as suggested by Bell et al. (2003).

FTIR results on crystals prior to shock reveal variable hydrogen contents in the starting material as presented in Figure 2. For olivine K1, which was used for FPA-3811, FPA-3812, FPA-3813, and FPA-3814, a starting hydrogen content of approximately 69–96 ppm by weight H_2O equivalent was present with the highest hydrogen contents in the center of the discs. For olivine K2, which was used for FPA-3816, FPA-3817, and FPA-3818, the hydrogen content could not be directly determined due to the orientation of the olivine disks because quantitative determination of hydrogen content in olivine requires three perpendicular measurements in polarized infrared light (Libowitzky & Beran, 2006). Nonetheless, peaks characteristic of hydrogen incorporated into the olivine crystal lattice (Miller et al., 1987) are clearly visible in the FTIR spectra for both materials. The peak observed near 3,700 cm^{-1} indicates the presence of serpentine-group minerals, which are not observable in either electron or optical microscopy. FTIR measurements acquired on samples after annealing at 1300°C in gas-mixing furnaces but prior to shock did not contain any detectable hydrogen. The high density of post-shock fractures prohibited quantitative determination of H contents using FTIR spectroscopy.

2.2. Electron Probe Microanalyses

Electron probe microanalyses (EPMA) were performed using a Cameca SX100 to measure the major element composition of the starting material prior to shock. Samples were prepared as for EBSD analyses, but thicker carbon coats of ∼15 nm were deposited on the surface of the samples prior to analyses. Wavelength dispersive spectroscopy data were collected using an accelerating voltage of 15 kV and a current of 20 nA. Standards used for EPMA included olivine from the Marjhalati meteorite (for Si, Fe, and Mg), oligoclase (for Al), diopside (for Ca), rutile (for Ti), nickel oxide (for Ni), chromite (for Cr), and rhodonite (for Mn). The measured concentrations of elements in the olivine crystals were determined based on those measured in the standards at the same conditions using Cameca processing routines and the PAP correction procedure (Pouchou & Pichoir, 1984). The chemical homogeneity of the samples was determined by making two perpendicular EMPA line profiles across the length of each crystal. Each line profile consisted of between 10 and 68 EMPA. The wt. % total for each analysis deviated less than 1% from the expected total of 100%. The standard deviation for each element is less than 0.5 weight %. Mn and Fe had detection limits below 0.07 weight %, and all other elements analyzed had detection limits below 0.05 weight %.

Table 1
Major Element Compositions

Oxide	K1 (wt.%)	Std. dev.	K2 (wt.%)	Std. dev.
SiO_2	41.44	0.19	41.05	0.16
MgO	54.22	0.34	50.27	0.27
FeO	4.18	0.34	8.53	0.27
CaO	0.01	0.01	0.01	0.01
TiO_2	0.01	0.01	0.01	0.01
MnO	0.17	0.02	0.16	0.02
Al_2O_3	0.00	0.00	0.00	0.03
Cr_2O_3	0.01	0.01	0.01	0.02
NiO	0.34	0.03	0.34	0.04
Total	100.36	0.30	100.36	0.30
Fo#	95.86	0.04	91.31	0.29

Note. Electron microprobe results of olivine crystals K1 (mean of 20 measurements) and K2 (mean of 106 measurements).

Average values of EPMA for the crystals prior to shock are presented in Table 1. The results reveal forsterite contents (Fo #) of 95.9 for K1 and 91.3 for K2 and homogeneous compositions throughout the crystals.

2.3. Electron Backscatter Diffraction

Analyses were carried out on an Oxford Instruments Symmetry EBSD detector mounted on a JEOL 7600F field emission scanning electron microscope and were processed using the Aztec software suite. The sample was tilted to 70° with respect to the detector during data collection. For each analysis,

EBSD maps of 180 × 250 μm^2 were acquired in the representative area near the center of the surface of the shocked crystals and away from any macroscopically apparent large fractures (the optical images in the data depository (https://doi.org/10.17605/OSF.IO/RXZ83) provide example photographs of four samples giving examples of fracture distribution generated during our experiments). Orientations were calculated by matching measured Kikuchi patterns to a forsterite index file (a = 4.75 Å, b = 10.20 Å, and c = 5.98 Å). Beam conditions were 20 kV and 10 nA for standard EBSD analyses and 25 kV and 10 nA for transmission Kikuchi diffraction (TKD) analyses. A working distance of 18–20 mm was used for most analyses. Indexing of crystallographic orientations was also attempted for the high-pressure polymorphs of olivine, wadsleyite, and ringwoodite, but results for those phases did not yield correct solutions for any of the samples.

2.4. Geometrically Necessary Dislocations

The density and character of GNDs were calculated using MTEX 5.2.8 (Bachmann et al., 2010) for MATLAB 2019b for EBSD data collected using a 1 μm step over a 250 × 180 μm^2. Analyses were attempted using a 0.1 μm step size but resulted in a high noise floor (see, e.g., Jiang et al., 2013). Calculations of GND content have been carried out by other workers using EBSD analyses acquired with high angular resolution (HR-EBSD) (Wallis et al., 2016; Wilkinson, 2001), which allows for the observation of low dislocation densities but requires specialized calibrations and proprietary software. The calculation of GNDs using Hough-based data, such as those acquired in this study, requires the removal of noise introduced during acquisition. The data were noise reduced

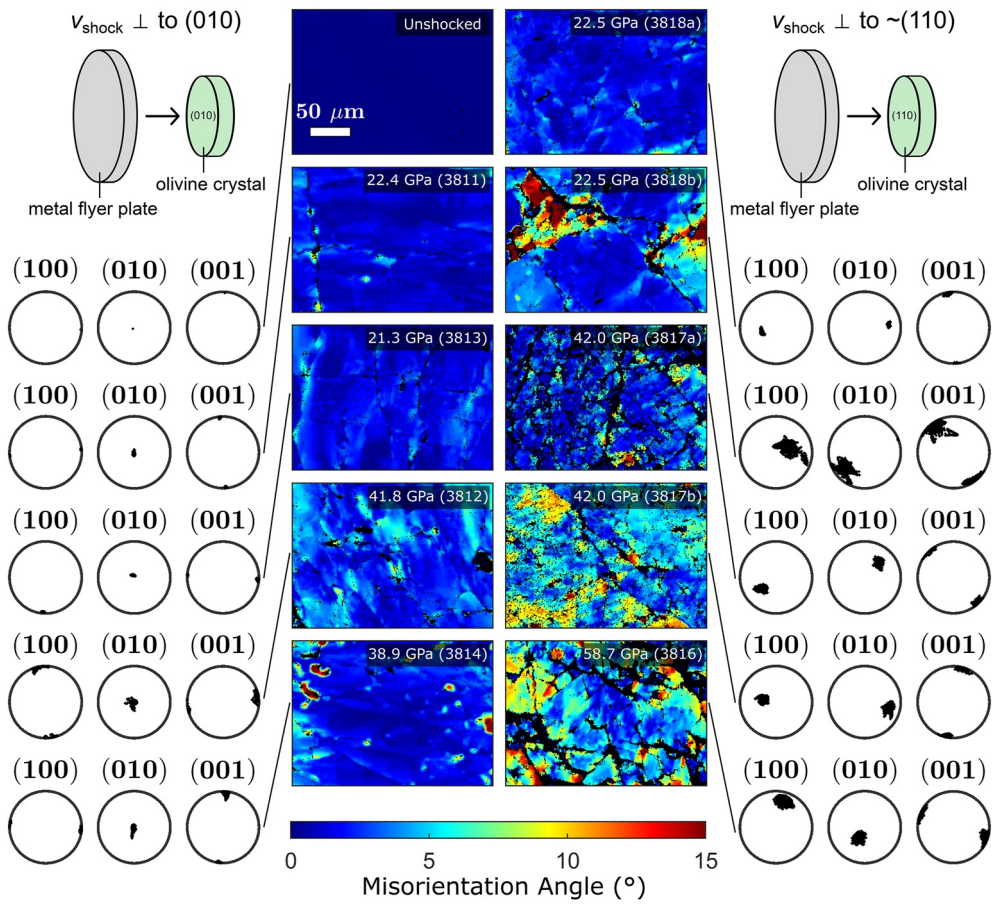

Figure 3. Maps of misorientation of each pixel relative to the mean orientation of the entire electron backscatter diffraction (EBSD) map for crystals shocked in the $[010]_c$ orientation on the left column and those shocked in the $[110]_c$ orientation on the right column. Black areas in the maps represent unindexed regions. Pole figures are lower hemisphere projections of crystallographic orientations for all indexed points on the corresponding maps. To verify the sample orientation relative to the impactor's direction, EBSD data were acquired along the plane of impact near the center of the sample.

Table 2
Mean Geometrically Necessary Dislocations (GND) for the Dominant Slip Systems for Experimentally Shocked Olivine Crystals

Mean GND density (m^{-2})[a]											
Experiment	*P* (GPa)	Crystal	Orientation	Annealed?	(010)[100]	(001)[100]	[100] Screw[b]	(010)[001]	(100)[001]	[001] Screw	Total
Unshocked	0	K1	$[010]_c$	No	4.15E+10	5.71E+10	1.96E+10	3.36E+10	8.05E+10	4.93E+10	2.82E+11
FPA-3811	22.4	K1	$[010]_c$	Yes	2.19E+12	1.80E+12	1.65E+12	4.05E+12	2.16E+12	2.80E+12	1.47E+13
FPA-3812	41.8	K1	$[010]_c$	Yes	5.62E+12	5.42E+12	3.35E+12	7.70E+12	4.54E+12	6.49E+12	3.31E+13
FPA-3813	21.3	K1	$[010]_c$	No	3.25E+12	2.64E+12	2.19E+12	4.12E+12	1.97E+12	3.54E+12	1.77E+13
FPA-3814	38.9	K1	$[010]_c$	No	3.13E+12	3.07E+12	2.30E+12	5.65E+12	4.43E+12	4.04E+12	2.26E+13
FPA-3816	58.7	K2	$[110]_c$	Yes	1.10E+13	1.13E+13	7.64E+12	1.16E+13	1.30E+13	1.26E+13	6.70E+13
FPA-3817a[c]	42.0	K2	$[110]_c$	No	1.95E+13	1.48E+13	1.11E+13	1.45E+13	1.20E+13	1.39E+13	8.59E+13
FPA-3817b[c]	42.0	K2	$[110]_c$	Yes	1.50E+13	1.13E+13	9.56E+12	1.07E+13	1.15E+13	1.26E+13	7.06E+13
FPA-3818a[c]	22.5	K2	$[110]_c$	No	8.26E+12	6.26E+12	5.05E+12	6.96E+12	5.60E+12	6.28E+12	3.84E+13
FPA-3818b[c]	22.5	K2	$[110]_c$	Yes	6.87E+12	6.89E+12	4.36E+12	6.54E+12	5.04E+12	5.21E+12	3.49E+13

[a]All data in the table were from electron backscatter diffraction maps measured with a 1 μm step size over a 180 × 250 grid. [b]Screw refers to screw dislocations while the others are edge dislocations. [c]Note that FPA-3817 and 3818 contained two half discs of natural and annealed olivine, which are labeled "a" and "b," respectively.

using a spline filter to preserve orientation gradients while removing noise introduced during data acquisition (Hielscher et al., 2019). The half-quadratic minimization method with an alpha value of 0.025 yielded similar results to data processed using a spline filter but had a higher noise floor and resulted in minor artifacts near fractures. The noise floor, estimated from GND calculations on the crystals before they were shocked, was lower by more than a factor of 10 than the lowest densities calculated for shocked crystals. The MATLAB script and EBSD data used to calculate GND densities for the shocked olivine crystals are available at the Open Research Framework website (https://doi.org/10.17605/OSF.IO/RXZ83). The method was confirmed as producing accurate estimates of both the type and the density of GNDs in a single crystal compressed under well-controlled (but lower stress) conditions (Supporting Information S1).

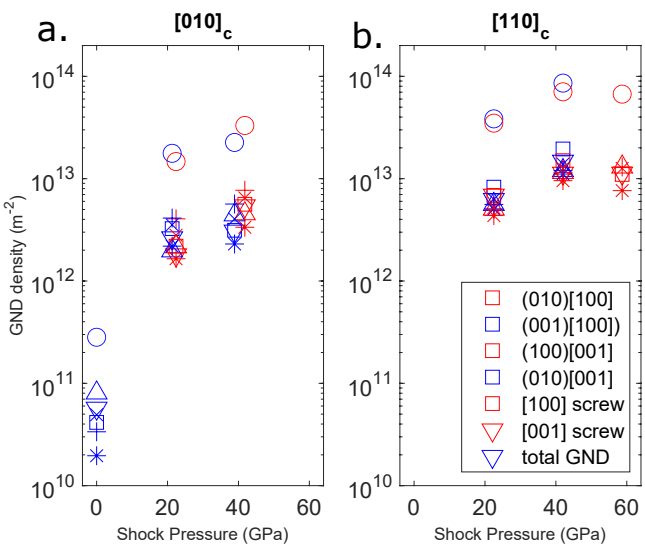

Figure 4. Mean geometrically necessary dislocations (GND) density versus peak shock pressure for olivine experimentally shocked in the $[010]_c$ orientation (a) and those shocked in the $[110]_c$ orientation (b).

2.5. Raman Spectroscopy

Raman spectroscopy is a vibrational spectroscopy technique that probes the frequency of molecular vibrations and phonons in crystals. The inelastically Raman-scattered light is frequency shifted from the monochromatic incident light. The frequency shift corresponds to the frequency of a normal mode vibration in the analyzed material. The most intense Raman bands in the olivine Raman spectrum and the bands of interest in this work are found at ~825 and ~865 cm^{-1} corresponding to the asymmetric and symmetric stretching modes of SiO_4^{4-} (Mouri & Enami, 2008). Local stress deviations near dislocations are associated with strain gradients (Peach & Koehler, 1950) that result in changes in molecular vibrational energies, which result in a shift in Raman band frequencies near dislocation cores in Raman spectra (Irmer & Jurisch, 2007; Kokubo et al., 2018). Raman analyses were performed using a WITec α-300R confocal Raman microscope (XMB3000-3003). Laser excitation was supplied via a 488-nm WITec diode laser (XSL3100-1155) with a power of ~15 μW at the sample focused to a beam diameter of ~3 μm for 120 s using a 20× objective. Between 10 and 12 Raman spectra were collected over various parts of the sample and away from the fractures. The Raman-scattered light was dispersed using a UHTS600 spectrometer with a 1,200 g/mm grating (WITec, XMC3200-0600) and detected by a back-illuminated charge-coupled device thermoelectrically cooled to −60°C. The wavenumber (Jakubek & Fries, 2020) and bandwidth (Jakubek & Fries, 2021)

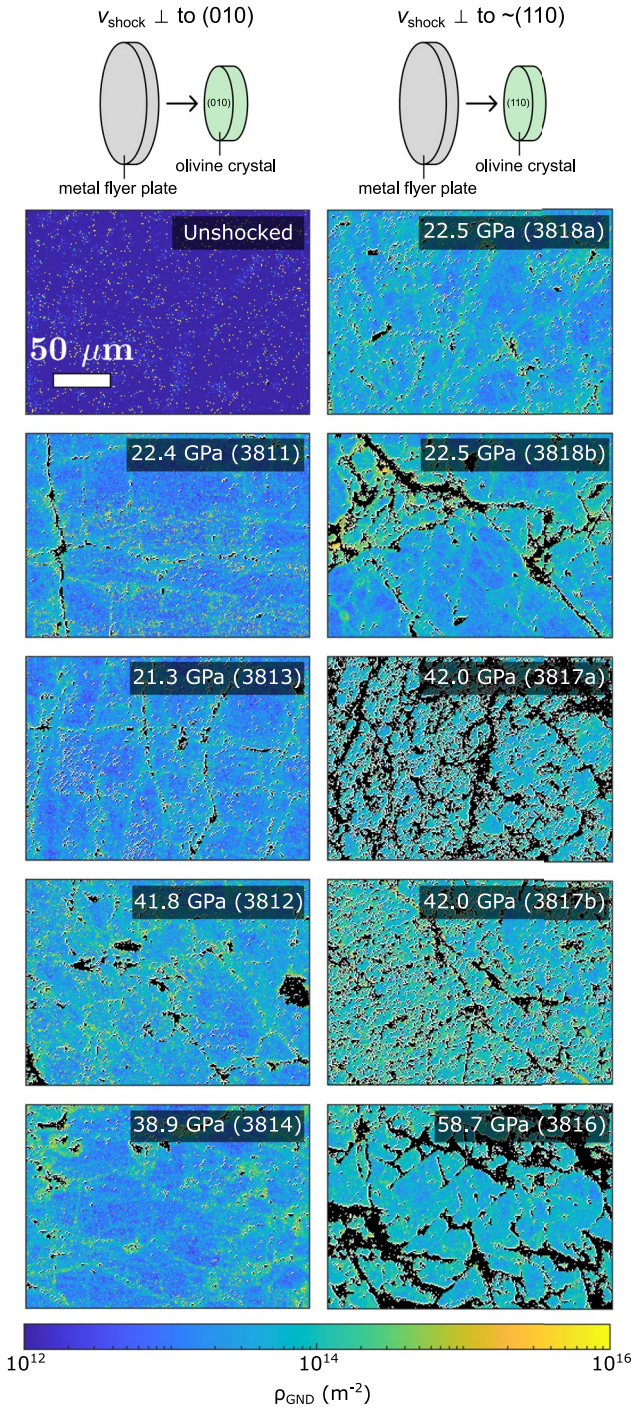

Figure 5. Maps of total geometrically necessary dislocations density (ρ_{GND}) for the experiments presented in Table 2 and Figure 3. Maps on the left column are for olivine K1 crystals shocked in the $[010]_c$ orientation and those in the right column are for olivine K2 crystals shocked in the $[110]_c$ orientation. To verify the sample orientation relative to the impactor's direction, electron backscatter diffraction data were acquired along the plane of impact near the center of the sample.

precision of our Raman instrument were previously found to be ~±0.15 and ~±0.1 cm^{-1}, respectively, without the use of advanced calibration techniques.

2.6. Transmission Electron Microscopy

TEM analyses were conducted to directly image the dislocation substructures producing some of the features observed in the EBSD maps. Sample preparation utilized focused ion beam (FIB) cross-sectioning techniques performed with FEI Quanta 3D dual electron/Ga^+ ion beam instrument. Final-stage Ga^+ ion milling used a sequence of progressively lower accelerating voltages, beginning with 30 kV and finishing as low as 2 kV, to minimize ion damage to the electron transparent areas of the samples. TEM employed both conventional bright-field/dark-field diffraction contrast imaging and scanning transmission electron imaging using a JEOL 2500SE 200 kV field-emission scanning transmission electron microscope.

3. Results

3.1. Electron Backscatter Diffraction Analyses

Data acquired from EBSD measurements reveal the development of shock-induced misorientation in olivine crystals. For unshocked olivine crystals, the degree of misorientation for each measured data point relative to the mean orientation of all measured points is less than 1° across a 180 × 250 μm^2 area as presented in Figure 3. In contrast, some of the shocked olivine crystals reveal misorientations exceeding 15° with the samples shocked to the highest shock pressure (58.7 GPa) having the largest degree of misorientation. Lower hemisphere pole figures representing the orientation of each measured point in the EBSD maps in Figure 3 reveal that shocked crystals have more diffuse point maxima of the principal crystallographic axes compared to the unshocked starting material.

The degree of misorientation depends on the relationship between the orientation of the crystal relative to the orientation of shock wave propagation. Crystals shocked in the $[010]_c$ orientation (left side of Figure 3) reveal smaller degrees of misorientation for a given shock pressure relative to crystals that were shocked in the $[110]_c$ orientation (right side of Figure 3).

3.2. Variation of GND Density With Shock Pressure

Calculations of GNDs from EBSD data reveal a range of densities and dislocation types develop in shocked crystals as presented in Table 2. The mean GND density cumulated over all slip systems varies from 2.82 × 10^{11} m^{-2} for unshocked crystals to 8.59 × 10^{13} m^{-2} for shocked crystals. The GND densities increase with increasing shock pressure for crystals shocked in the same orientation. However, a slight decrease in the dislocation density occurs for some slip systems between shock pressures of 42.0 and 58.7 GPa for crystals in the $[110]_c$ orientation. The mean GND density for each slip system varies systematically as a function of peak shock pressure as presented in Figure 4.

3.3. Distribution of GNDs in Shocked Crystals

The distribution of total GNDs in shocked samples is locally heterogeneous as presented in Figure 5. Linear features of relatively high GND density occur

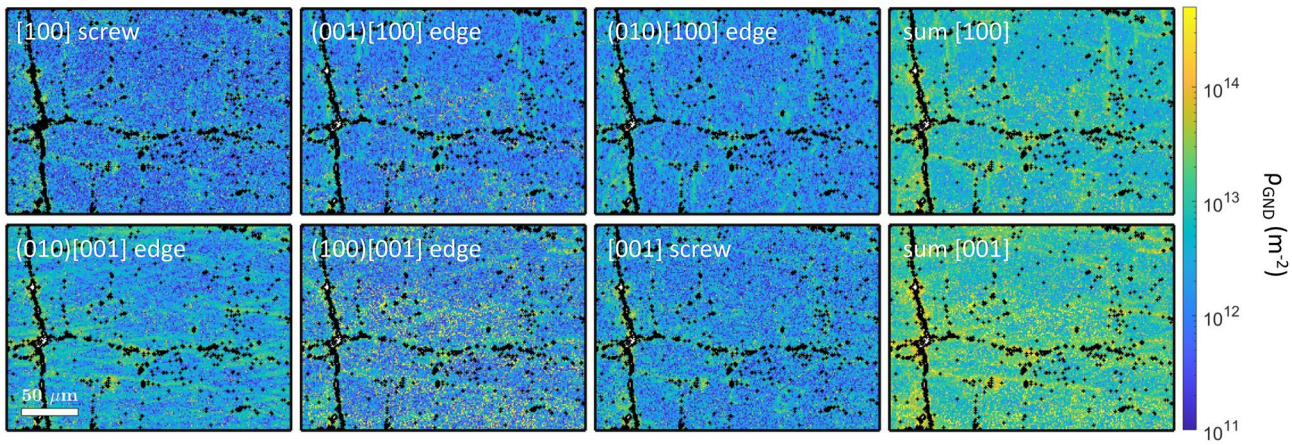

Figure 6. Maps of the density of geometrically necessary dislocations (GNDs) from a K1 olivine crystal that was annealed and then shocked in the $[010]_c$ orientation at a peak shock pressure of 22.4 GPa in experiment FPA-3811. To verify the sample orientation relative to the impactor's direction, electron backscatter diffraction data were acquired along the plane of impact near the center of the sample.

in most of the samples and often form parallel to (100) and (001). Linear features consisting of high GND density are also observed forming oblique to the principal crystallographic axes and commonly on (031). The GND density is also observed to be larger near fractures in many samples.

Closely spaced (<30 μm) repeating bands of dislocations occur in some samples as presented in Figure 6. These bands consist primarily of (010)[001] and (100)[001] edge dislocations and have densities ranging from less than 10^{12} m^{-2} to greater than 10^{14} m^{-2}.

3.4. Influence of Crystallographic Orientation on Dominant Burgers Vector Type

The types of dislocations present in shocked crystals are dependent on the orientation of individual dislocation slip systems relative to the orientation of shock wave propagation. The Schmid factor (S) describes the relationship between the orientation of applied force (F) with respect to the orientation of a vector normal to the slip plane (n) and the burgers vector such that

$$S = \cos(\alpha)\cos(\beta), \quad (1)$$

where α is the angle between F and n and β is the angle between F and b (Schmid & Boas, 1935). Values of S range from 0 for a dislocation slip system that is poorly oriented for dislocation motion to 0.5 for a perfectly oriented slip system. It therefore follows that each dislocation slip system in each grain will have a different value of S when a plastic deformation wave moves through a polycrystalline sample. Variations in the orientation of F, such as at interfaces or fractures, will result in different values of S, therefore activating different slip systems.

Table 3
Schmid Factors Calculated for the Dominant Olivine Dislocation Slip Systems

Values of mean Schmid factor for shocked olivine[a]						
	P (GPa)	Crystal	Annealed?	(010) [100]	(010) [001]	(001)[100] and (100) [001]
Unshocked	0	K1	No	0.055	0.051	0.003
FPA-3811	22.4	K1	Yes	0.010	0.046	0.000
FPA-3812	41.8	K1	Yes	0.012	0.048	0.001
FPA-3813	21.3	K1	No	0.091	0.108	0.010
FPA-3814	38.9	K1	No	0.013	0.189	0.003
FPA-3816	58.7	K2	Yes	0.290	0.028	0.009
FPA-3817a	42.0	K2	No	0.436	0.033	0.057
FPA-3817b	42.0	K2	Yes	0.491	0.048	0.056
FPA-3818a	22.5	K2	No	0.491	0.038	0.045
FPA-3818b	22.5	K2	Yes	0.460	0.033	0.050

[a]The direction of shock wave propagation was assumed to be parallel to the orientation of maximum compressive stress when calculating the Schmid factor.

The Schmid factors for the dominant dislocation slip systems in olivine for each experiment are presented in Table 3. Experiments that were derived from olivine K1 (FPA-3811, FPA-3812, FPA-3813, and FPA-3814) have low Schmid factors for all slip systems, whereas those derived from olivine K2 (FPA-3816, FPA-3817, and FPA-3818) have high values of Schmid factor for the (010)[100] slip system and low values for all other slip systems.

Different types of GNDs are present in the shocked material as presented in Figure 7. For crystals that were shocked with the direction of shock wave propagation normal to (010), (010)[001] edge GNDs are most common. For crystals shocked with the direction of shock wave propagation approximately

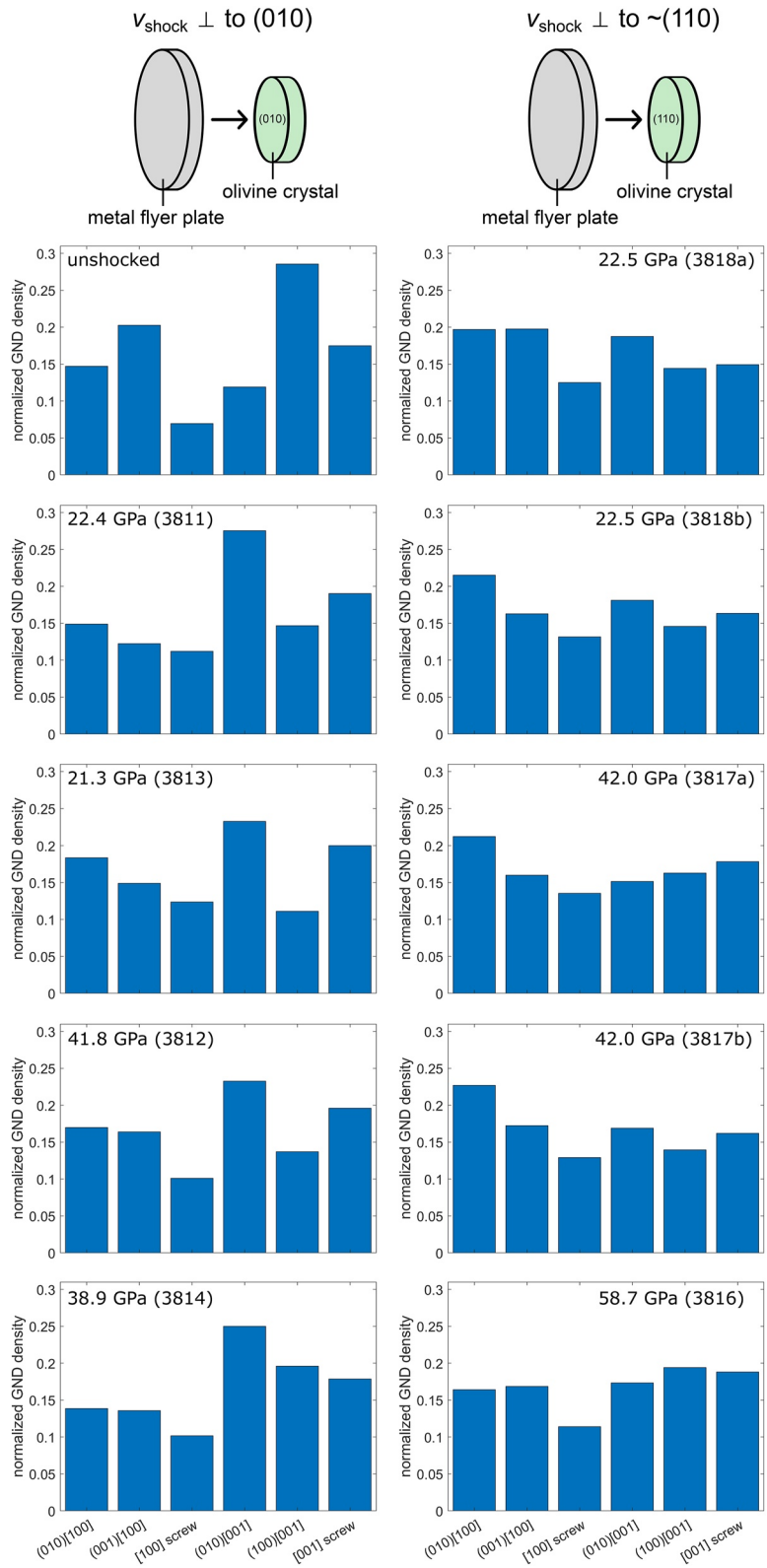

Figure 7. Abundance of geometrically necessary dislocations (GNDs) on each slip system normalized to the total GND density for all slip systems for each sample. Plots on the left column are for crystals shocked in the $[010]_c$ orientation and those on the right column were shocked in the $[110]_c$ orientation. Dislocations with $b = [100]$ are relatively more common in crystals shocked in the $[110]_c$ orientation than those shocked in the $[010]_c$ orientation. Similar relative GND abundances are present in annealed and untreated crystals shocked at similar conditions.

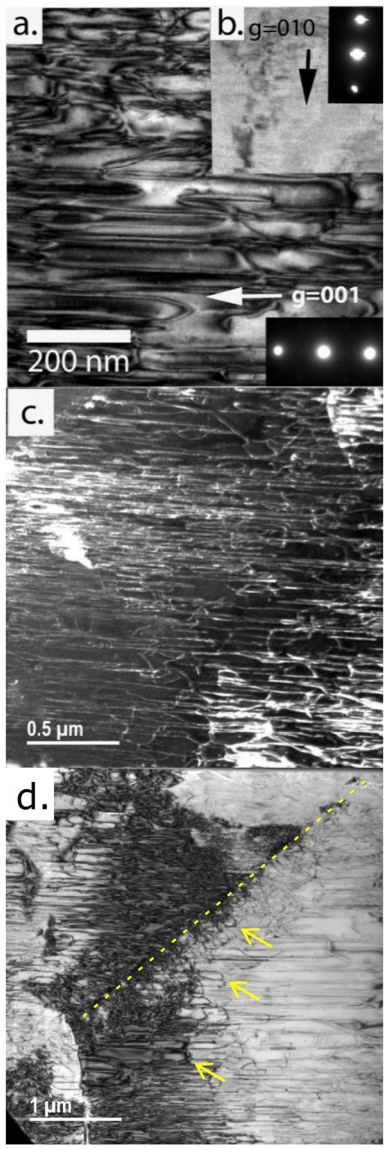

Figure 8. Conventional diffraction contrast transmission electron microscopy (TEM) images of dislocation substructures in the FIB section of annealed (dehydrated) olivine K2 that was shocked at 58.7 GPa (FPA-3816). (a) Conventional bright-field image acquired under approximate two-beam conditions for $g = 001$ along the 00l systematic row of reflections. (b) Conventional bright-field image of parallel dislocation array adjacent to panel (a) showing near total extinction under two-beam imaging conditions for $g = 010$, consistent with Burgers vector $b = [001]$ (c-axis). (c) Conventional TEM image of area adjacent to panel (b) under "weak-beam" dark-field conditions for diffraction along $g = 001$ systematic row showing details of dislocation sub-structure under reduced strain-contrast imaging conditions. (d) Conventional bright-field image taken under symmetrical [100] zone axis diffraction conditions showing gradation in dislocation density adjacent to low-angle grain boundary. Most of the horizontal lines are screw dislocations with $b = [001]$, examples of the ends of dislocations loops are indicated by the yellow arrow, and the trace of a fracture with orientation near (031) is highlighted by the dashed yellow line in panel (d).

normal to (110), the (010)[100] edge GND slip systems are more common. The exception to the dominance of (010)[100] edge GNDs in crystals shocked in that the orientation is for FPA-3816, which was shocked at the highest pressure (58.7 GPa), and has a lower Schmid factor for (010)[100] compared to the other crystals shocked in that orientation (i.e., K2 crystals shocked in the $[110]_c$ orientation) as presented in Table 3. Little variation in the distribution of dislocation types is observed when comparing shocked crystals that contained hydrogen to those that were dehydrated by annealing at high temperature prior to shock (Figure 7).

3.5. Transmission Electron Microscopy

Details of the dislocation substructure in the inter-boundary regions of the highest shocked sample as well as the structure of the boundaries themselves are shown in TEM images in Figure 8. Figure 8 details the key characteristic of much of the dislocation substructure throughout the inter-boundary region of the sample: high dislocation density (1×10^{14} to 2×10^{14} m^{-2}) arrays of parallel dislocation lines oriented along [001]. Two-beam $\mathbf{g} \bullet \mathbf{b}$ diffraction contrast experiments performed using systematic rows of reflections in [100] zone axis diffraction patterns showed near total extinction of the parallel dislocation arrays for $\mathbf{g} = h00$ (see Figure 8b inset), but strong contrast for $\mathbf{g} = 00l$. The results confirm that most, if not all, of the visible dislocations in the TEM images of the FIB section have Burgers vectors parallel to [001]. The orientation of the dislocation lines also along [001] suggests that the arrays are dominated by screw-component dislocations that are part of highly elongate dislocation loops with short edge components.

3.6. Transmission Kikuchi Diffraction

TKD analyses were carried out on a FIB foil extracted at the interface between hydrous and anhydrous olivine in diffusion couple experiment FPA 3817, which was impacted at a peak shock pressure of 42.0 GPa. The TKD results reveal the presence of fine-grained olivine crystals that are present at the interface between the two crystals and confirmed by TEM analyses as presented in Figure 9. The smaller olivine grains have a relatively uniform orientation distribution (Figure 9) and contain low values of internal misorientation (Figure 9). In addition, they appear to have lower fracture densities, compared to the two large crystals that made up the initial diffusion couple, and they generally display curved grain boundaries.

3.7. Raman Measurements

Raman measurements carried out on oriented sections of the starting material and shocked olivine crystals are presented in Figure 10. Characteristic olivine Raman bands occur at 825, 857, 882, 919, and 961 cm^{-1}. For all samples, the 825 and 857 cm^{-1} asymmetric and symmetric Si-O stretching bands are the most prominent. For spectra collected on the (010) plane, the peak at 919 cm^{-1} is not observed. For each sample, 10–12 Raman spectra were collected at different locations of the sample. In general, the variation between the FWHH of Raman spectra collected from each sample given increases, and the signal-to-noise ratio (S/N) of the Raman spectra decreases with increasing shock pressure.

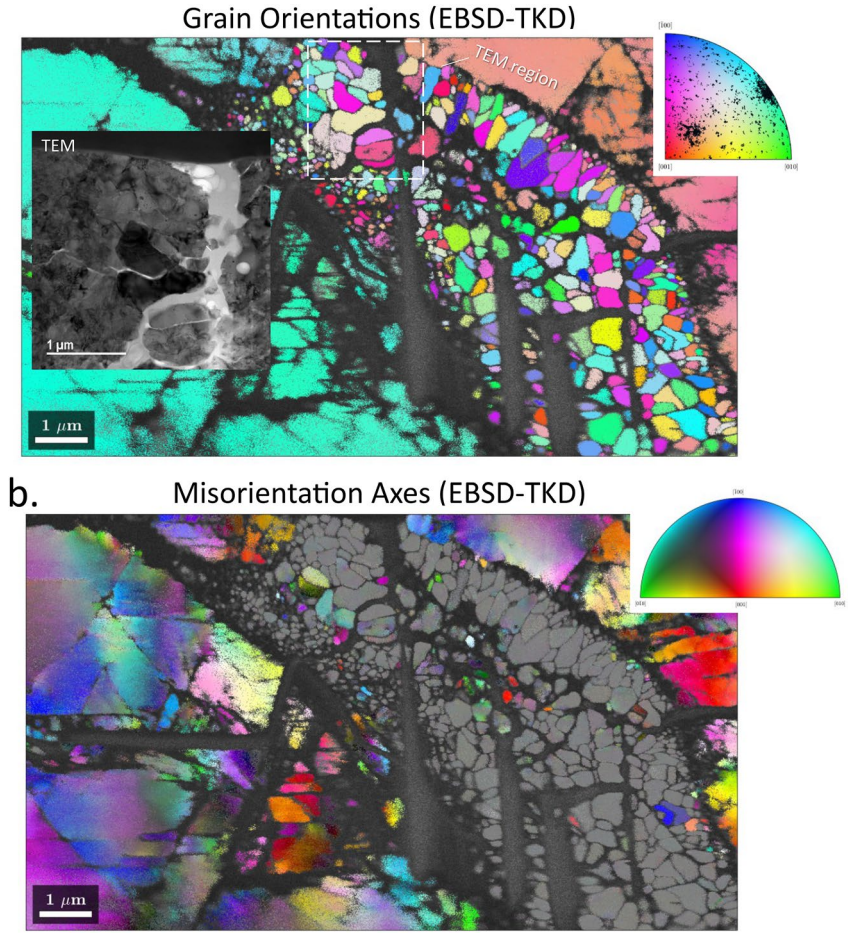

Figure 9. Results from transmission Kikuchi diffraction analyses at the interface of hydrous and anhydrous crystals in a diffusion couple that were impacted at a peak pressure of 42.0 GPa (FPA-3817). (a) Grain orientation map with crystallographic directions mapped to the *z*-axis inverse pole figure in the top right. A region of fine-grained olivine is present and further confirmed by transmission electron microscopy analyses in the inset image (the light regions are epoxy). (b) Misorientation axes map with the direction of misorientation in each grain mapped to the inverse pole figure in the top right. The grains in the fine-grained regions reveal a lack of misorientation compared to the larger crystals on the left and right sides of the image.

Results from fitting a Lorentzian function to the 825 and 857 cm^{-1} peaks are presented in Table 4. The positions of the 825 and 857 cm^{-1} peaks vary by <0.25 cm^{-1} but not systematically with increasing peak shock pressure for either crystals shocked in the $[010]_c$ orientation or those shocked in the $[110]_c$ orientation. In contrast, the FWHH of the peaks increase systematically with increasing peak shock pressure. Values of FWHH for the 825 cm^{-1} peaks range from 8.358 cm^{-1} for unshocked crystals to 11.379 cm^{-1} for those shocked at 58.7 GPa. For the peak at 857 cm^{-1}, values of FWHH range from 8.931 cm^{-1} for unshocked crystals up to 12.755 cm^{-1} for those shocked at 58.7 GPa.

The FWHH of the 825 and 857 cm^{-1} peaks in Raman spectra can be fit to a linear relationship such that

$$\text{FWHH} = P \times m + w, \tag{2}$$

where P is the peak pressure in GPa, and both m and w are constants that depend on the wavenumber of the peak and the orientation of the crystal relative to the direction of shock wave propagation as presented in Figure 11. Values of m for the 825 cm^{-1} peak range from 0.023 for crystals shocked in the $[010]_c$ orientation to 0.047 for crystals shocked in the $[110]_c$ orientation. For the 857 cm^{-1} peak, values of m range from 0.029 for crystals shocked in the $[010]_c$ orientation to 0.038 for crystals shocked in the $[110]_c$ orientation. Values of m are therefore

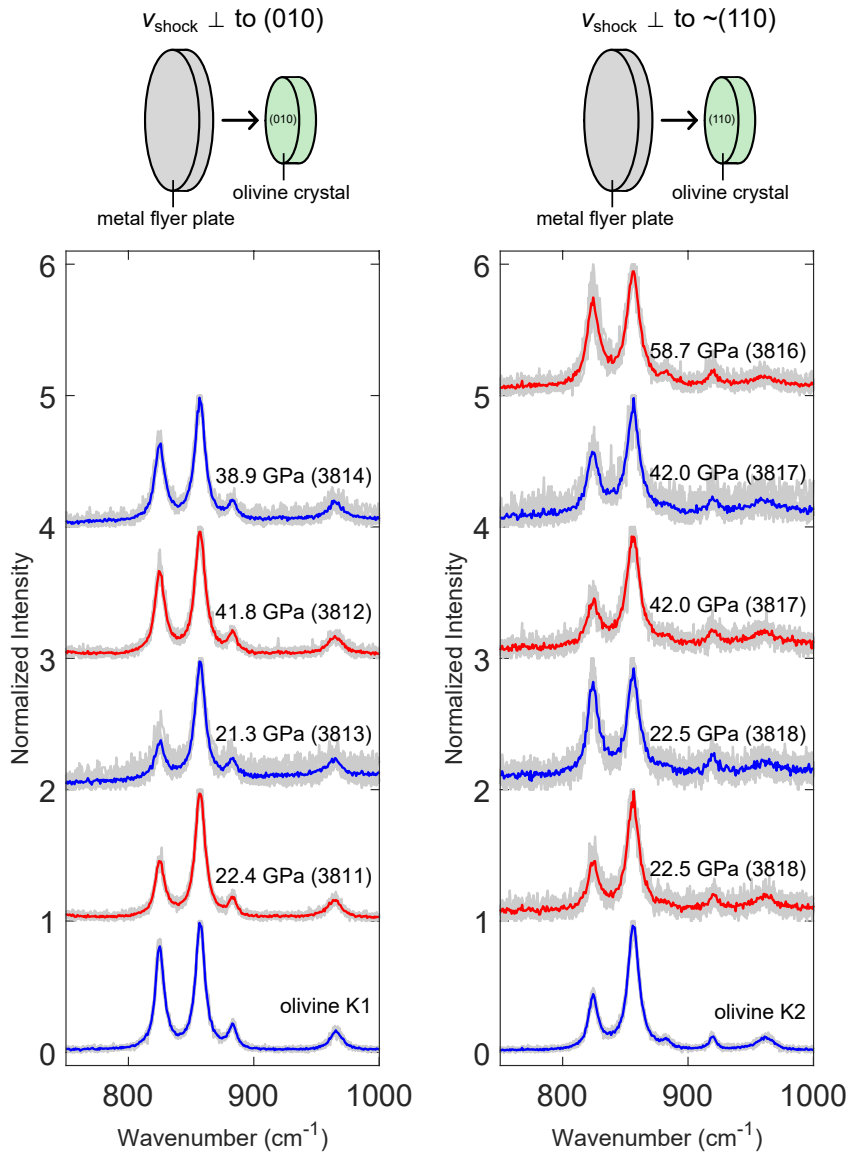

Figure 10. Raman spectra collected over the 750–1,000 cm^{-1} spectral range for olivine crystals. Gray lines represent 10–12 individual measurements on each sample, red lines represent the mean of all measurements for annealed (i.e., anhydrous) samples, and blue lines represent the mean of all measurements for non-annealed (i.e., hydrous) samples. The spectral intensities were normalized to the 856 cm^{-1} band for clarity.

smaller in crystals shocked in the $[010]_c$ orientation than for those shocked in the $[110]_c$ orientation. The values of FWHH of these peaks do not depend on whether the sample was annealed for dehydration prior to shock as presented in Figure 11.

The FWHH values reported in Table 4 and Figure 11 are those directly observed in the Raman spectrum. However, the Raman bandwidth observed in a Raman spectrum is distorted by the spectrometer slit function. Thus, to compare Raman bandwidths across instruments, one needs to calibrate for the effects of the spectrometer slit. In Supporting Information S1, we describe, in detail, our calibration procedure. We find that the calibrated intrinsic Raman bandwidths to be ~1%–4% smaller than the uncalibrated bandwidths (Table S1 in Supporting Information S1).

Table 4
Mean Values of Position (i.e., Raman Shift) and Full Width at Half Height (FWHH) for Shocked Crystals and the Starting Material

Experiment	*P* (GPa)	Position (cm^{-1})	FWHH (cm^{-1})	Position (cm^{-1})	FWHH (cm^{-1})
K1 (unshocked)	0	824.937 (0.073)	8.358 (0.15)	857.278 (0.061)	8.931 (0.189)
FPA-3811	22.40	825.092 (0.209)	9.386 (0.592)	857.209 (0.209)	9.570 (0.335)
FPA-3812	41.80	824.995 (0.176)	9.627 (0.765)	857.176 (0.116)	10.550 (0.946)
FPA-3813	21.30	825.078 (0.325)	9.544 (1.555)	857.168 (0.282)	9.677 (0.821)
FPA-3814	38.90	824.968 (0.185)	9.165 (0.504)	857.098 (0.164)	9.610 (0.392)
K2 (unshocked)	0	824.411 (0.142)	9.282 (0.400)	856.392 (0.097)	10.781 (0.171)
FPA-3816	58.70	824.285 (0.279)	11.379 (0.852)	856.217 (0.237)	12.755 (0.850)
FPA-3817 wet	41.96	824.369 (0.205)	10.803 (0.763)	856.239 (0.178)	11.970 (0.684)
FPA-3817 dry	41.96	824.424 (0.699)	11.015 (1.089)	856.216 (0.277)	12.509 (1.015)
FPA-3818 wet	22.53	824.207 (0.219)	9.577 (0.516)	856.285 (0.217)	10.832 (0.693)
FPA-3818 dry	22.53	824.452 (0.327)	8.816 (0.589)	856.160 (0.208)	11.008 (0.681)

Note. Values are from fitting a Lorentzian relationship to Raman spectra for a minimum of 10 spectra measurements from different regions on each sample. The standard deviation of each mean value is in parentheses.

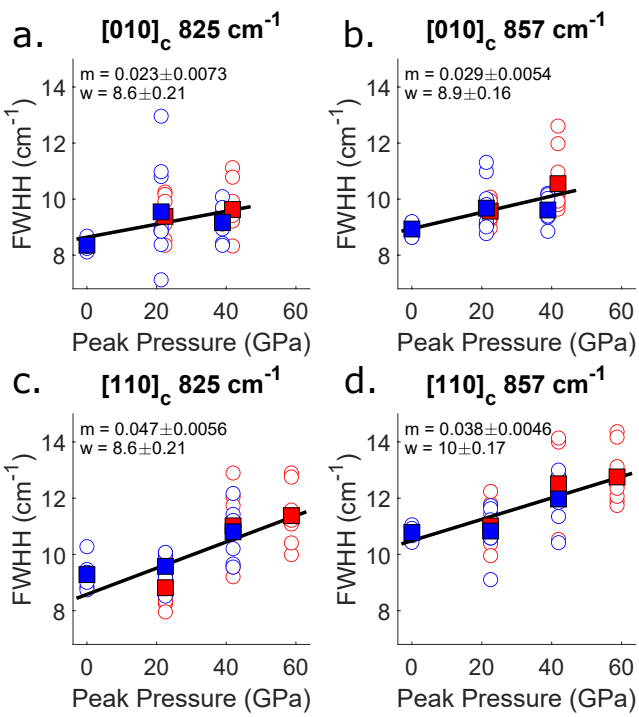

Figure 11. Variation in full width half height (FWHH) of the 825 and 857 cm^{-1} bands in Raman spectra for experimentally shocked olivine crystals. Data from crystals in the $[010]_c$ orientation relative to the shock wave are in panels (a and b) and those in the $[110]_c$ orientation are panels (c and d). The circles are for individual Raman spectra acquired from 10 to 12 different spots on each sample, the black lines are linear fits of Equation 2 to the all the data (not the mean values), where the values of *m* and *w* are displayed on each plot. The solid colored squares are the mean values of FWHH for each sample. Data for natural olivine are plotted with blue symbols and those for annealed olivine crystals are plotted as red.

4. Discussion

4.1. Variation of GND Density on Shock Pressure

The results presented in Figure 4 reveal an increase in GND density with increasing shock pressure between 20 and 40 GPa for crystals shocked in either the $[010]_c$ or the $[110]_c$ orientations. The exception to the observed increase in GND density with increasing shock pressure is FPA-3816, which was shocked at the highest peak pressure (58.7 GPa), and has a lower GND density than crystals that were shocked in the same orientation but at a peak pressure of 42.0 GPa (Table 2). The lack of increase in GND density with increasing shock pressures above ~40 GPa suggests that a change in the mechanism of dislocation generation occurs at high shock pressure. At the highest peak pressures, closely spaced dislocation loops become more prevalent. The close spacing of dislocations with opposite line directions likely results in a local apparent "canceling out" of lattice strain, making measurements of GND content very difficult to determine with existing techniques. It is also possible that the repulsive stress of dislocation-dislocation interactions begins to saturate and balance the stress from the shock wave. It is worth noting that similar results have been observed in molecular dynamics simulations of dislocation development during the shock of copper single crystals (Sichani & Spearot, 2016). Copper crystals shocked parallel to {100} and {110} illustrate a large increase in dislocation density between 20 and 40 GPa shock pressure. A smaller increase in dislocation density and in some cases, a decrease in dislocation occur for copper crystals shocked in those orientations between 40 and 60 GPa shock pressure.

4.2. Influence of Crystallographic Orientation on Dislocation Density

Comparison of the total GND density for crystals shocked in different orientations in Table 2 reveals that for similar peak shock pressures, crystals shocked in the $[110]_c$ orientations have a factor of ~2.6 higher GND densities compared to crystals shocked in the $[010]_c$ orientations. The types of GNDs depend more strongly on grain orientation than on peak shock pressure

as presented in Figure 12. The ratio of GNDs with $b = [100]$ to those with $b = [001]$ does not vary systematically with peak shock pressure. In contrast, grains with high values of Schmid factor for (010)[100] have the highest ratios of GNDs with $b = [100]$ to those with $b = [001]$. This is consistent with the fact that dislocations in olivine form and move primarily on four slip systems: (010)[100], (001)[100], (010)[001], and (100)[001]. At high stress conditions, dislocations on the (010)[001] and (100)[001] slip systems have the highest velocities (Berg, 1974; Carter & Ave'Lallemant, 1970; Idrissi et al., 2016; Tielke et al., 2016). The relationships of GND density and orientation can be explained by the fact that GND on each slip system is controlled by a balance of stress that generates and moves dislocations and the interactive forces between dislocations that may cause them to either annihilate or repel each other.

For olivine deforming at steady-state conditions, the dislocation density (ρ) obeys a power-law dependence on stress (σ), such that

$$\rho = A\left(\frac{S}{b}\right)^{p}\left(\frac{\sigma}{\mu}\right)^{q}, \tag{3}$$

where A, p, and q are constants, S is the Schmid factor (Equation 1), b is the burgers vector, and μ is the shear modulus (e.g., Karato, 2012). Note that A is an empirical constant with units of Pa^{-q}. For the case of olivine deforming at steady-state conditions, q is approximately 1.4 (Bai & Kohlstedt, 1992; Hirth & Kohlstedt, 2015). For dislocations forming in plastic shock waves, values of q are less well established, but recent simulations of nucleation and propagation of dislocations in copper under shock compression reveal that dislocation densities increase with shock pressure to the power of ~0.6 (Shehadeh & Zbib, 2016). Our data are consistent with the operation of a mechanism to generate dislocations as described in Equation 3, where the deviatoric stress generated by shock waves is resolved onto each slip system. Dislocations on slip systems with low Schmid factors may be generated by dislocation multiplication or by local deviations in stress due to the presence of fractures or other defects.

4.3. Generation and Movement of Dislocations During Shock

To explain the formation of the microstructures observed by TEM and the concentration of dislocation loops along fractures, an understanding of the relation between shock wave propagation and dislocation mobility is necessary. When a shock wave (i.e., an elastic precursor) propagates through a crystalline material, a condition of uniaxial strain results in a concentration of deviatoric stress at the shock front. If the shock pressure exceeds the HEL of a crystal, then dislocations are generated and displaced, therefore forming a plastic shock front. The plastic strain rate ($\dot{\gamma}$) of a material undergoing deformation via the propagation of dislocations associated with a shock wave may be described using a modified version of the Orowan Equation (Orowan, 1940), such that

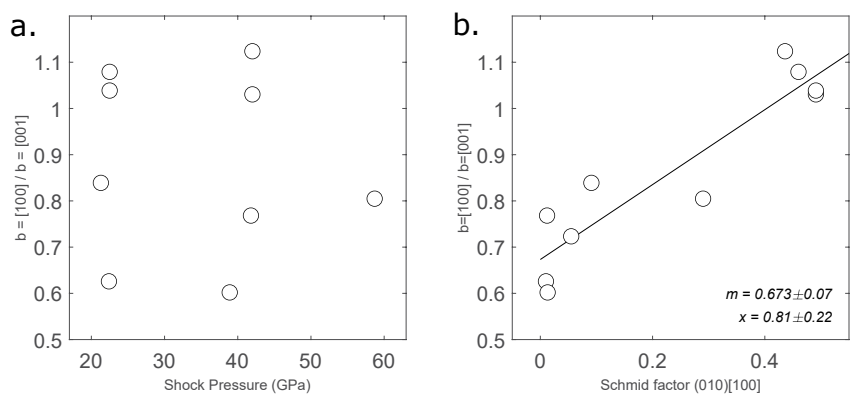

Figure 12. Variation in the ratio of geometrically necessary dislocation (GND) density for slip systems with $b = [100]$ to those with $b = [001]$ with shock pressure (left) and the Schmid factor for (010)[100] (right) within each sample. The black line is a linear fit to those data such that mean GND density of $b = [100]$/mean GND density $b = [001]$ is equal to $mx + b$, where x is the Schmid factor for the (010)[100] slip. Errors in m and b represent 90% confident bounds determined from fitting in a least squares regression.

$$\dot{\gamma} = \rho b \bar{v} + \dot{\rho} b \bar{l}, \tag{4}$$

where ρ is the dislocation density, b is the burgers vector, $\bar{v}$ is the mean velocity of dislocations, $\dot{\rho}$ is the rate of generation of dislocations, and $\bar{l}$ is the mean distance traveled by dislocations during the shock event (Meyers et al., 2009). For the case of mobile dislocations that are displaced in association with a shock wave, most of the strain is acquired through the velocity of dislocations, so the relationship can be approximated by the classic Orowan Equation:

$$\dot{\gamma} = \rho b \bar{v} \tag{5}$$

Under this condition, dislocations often form loops with their edge components moving in front of the shock front and their screw components left behind (Hornbogen, 1962; Smith, 1958), in which case the edge components travel at either sonic or supersonic velocities.

In contrast, if the dislocations that are generated by the elastic precursor are either immobile or have lower mobility than that of the elastic precursor, then the change in dislocation density that occurs behind the propagating shock wave results in the increase in strain rate through the orientation gradients caused by the presence of dislocations. For the case of shock-generated dislocations with low mobility, the strain rate is approximated by

$$\dot{\gamma} = \dot{\rho} b \bar{l}. \tag{6}$$

Dislocations may also be periodically generated near the shock front and either not propagated or propagated at subsonic velocities (Meyers, 1978). Dislocation loops may develop behind the elastic precursor and form stacking faults that result in the formation of twins in some materials (Zaretsky, 1995). The microstructure, in particular the loops observed in Figure 8, is consistent with glide conditions under which the edge components of dislocation loops have high mobility, but the screw components have low mobility possibility due to restricted cross-slip or dislocation interaction effects.

4.4. Relationship Between Planar Defects and Dislocation Density

The EBSD-GND results presented in Figures 5 and 6 and the TEM results presented in Figure 8 reveal that the highest dislocation densities are present along the edges of planar discontinuities in the sample, either grain boundaries in the case of the EBSD-GND results, but also low-angle grain boundaries as observed in the TEM results. A similar relationship was observed in an olivine single crystal experimentally shocked using a short pulse laser shock (Langenhorst et al., 1999) and a crystal shocked using an explosively propelled flyer plate to induce shear along fractures (Langenhorst et al., 2002). The coincidence of high dislocation densities near fractures led Langenhorst et al. (1999) to propose that the local stress field around Mode I (tensile) and Mode II (shear) fractures along (031) controls the generation of dislocations in shocked olivine, where the value of Schmid factor along fractures results in high-resolved shear stress on dislocations on (010)[001].

The results for crystals impacted in the $[010]_c$ orientation presented above are consistent with the results and interpretations of Langenhorst et al. (1999). Similar to the result of Langenhorst et al. (1999), whose olivine were shocked parallel to (001), all of the primary dislocation slip systems had macroscopic values of Schmid factor roughly equal to zero, and the dominant slip system for all cases was (010)[001]. Therefore, for crystals shocked in orientations that result in low values of Schmid factor, dislocation density appears strongly associated with the orientations of fractures. This relationship is likely due to a combination of local deviations in stress around propagating fractures and the preferred nucleation of dislocations along fractures or grain boundaries.

In contrast to crystals shocked in the $[010]_c$ orientations, the most common types of GNDs from crystals shocked in the $[110]_c$ orientations are (010)[100] edge dislocations. The higher dislocation density and the change in the type of dislocations for crystals shocked in that orientation suggest that different mechanisms of dislocation generation operate for crystals shocked in different orientations. It is likely that the process described by Langenhorst et al. (1999) where stress concentrations near fractures generate dislocations, and those described by Meyers (1978), where stress concentrations at the elastic precursor generate dislocations, may operate in parallel.

Dislocations with b = [001] are often generated at Mode I and II fractures along common fracture planes in olivine. In contrast, dislocations with b = [100] are generated at intracrystalline nucleation points, such as Frank-Read sources (Frank & Read, 1950), due to the deviatoric stress from the elastic precursor resolved on favorably oriented dislocation slip systems. We therefore propose that the total dislocation generation rate ($\dot{\rho}_{\text{tot}}$) for olivine crystals during shock is

$$\dot{\rho}_{\text{tot}} = \dot{\rho_f} + \dot{\rho}_e, \tag{7}$$

where $\dot{\rho_f}$ is the dislocation generation rate due to the propagation of Mode I and II fractures and $\dot{\rho}_e$ is the dislocation generation rate due to the deviatoric stress generated by the propagation of the elastic precursor.

4.5. Influence of Hydrogen Content on GND Density and Mobility

Both the EBSD and Raman data presented above reveal that the development of shock-induced dislocations is independent of hydrogen content of the starting material. This observation is consistent with the operation of dislocation generation presented in Equation 3, where the only hydrogen-sensitive parameter is the shear modulus, which has negligible variation for the range of hydrogen content investigated in these experiments (e.g., Jacobsen et al., 2008). These results are consistent with observations of dislocation densities that form under steady-state deformation conditions, where dislocation density does not vary as a function of hydrogen content in olivine crystals (Karato & Jung, 2003).

4.6. Limitations of the EBSD-GND Technique in Planetary Materials

It is important to note that the under certain conditions, the calculated values of mean GND density are likely lower than the actual values of dislocation density due to proximity of dislocations of opposite sign (e.g., Kubin & Mortensen, 2003). The difference between the GND density and the actual density is due to the prevalence of dislocation loops. As dislocation loops necessarily require dislocations with opposite sign, those dislocations will cancel each other out (in other words, they will not be geometrically necessary), if the loops have radii smaller (e.g., ∼50 nm; Figure 8) than the step size used in the EBSD data acquired for GND analyses (1 micron). Our analysis may thus underestimate the GND, and we thus did not attempt to quantify the relationships between GND and shock pressure shown in Figure 4. We note that the influence of dislocation loops on Raman spectra does not suffer from this artifact as the strain-dependent shifts in wavenumber in Raman spectra do not cancel each other out in the same way. Nonetheless, GND analyses provide information on dislocation types that can be collected over larger areas than TEM analyses.

4.7. Evidence for Partial Melting

The EBSD-TKD results presented in Figure 9 reveal the presence of fine-grained material at the interface between anhydrous and hydrous crystals that were shocked at 42.0 GPa (FPA-3817). The fine-grained material displays very low internal misorientation, a lack of internal fractures, and a nearly random distribution of crystallographic orientations. All these observations are consistent with the formation of very localized shock-induced melting at the interface between the two crystals that resulted in the nucleation and growth of the fine-grained olivine. The formation of the melt and subsequent crystallization of the new olivine grains likely immediately post-dated the traversing of the shock wave through the adjacent larger olivine crystals. Therefore, it is unlikely that the generation of melt along the interface of the two crystals influenced the movement of the elastic precursor through the crystals or the generation of dislocations during the shock event. Additionally, the melt-rich region that occupied the interface represented approximately 0.1% of the volume of the shocked olivine in the experiment and therefore only locally influenced dislocation generation of the sample. These observations are consistent with previous impact experiments on olivine (Langenhorst et al., 2002), basalt (Schaal et al., 1979) and lunar soil (Schaal & Horz, 1980), naturally shocked rocks on Earth (Kieffer, 1971) or as meteorites (Walton & Herd, 2007), the Moon (Kieffer, 1975), and modeling of pore collapse during the shock of crystalline material (Austin et al., 2014). Therefore, melt may be generated in materials that contain porosity or preexisting fractures, such as those generated from previous impact events on planetary samples and that care should be taken when interpreting shock pressures based on the presence of melt.

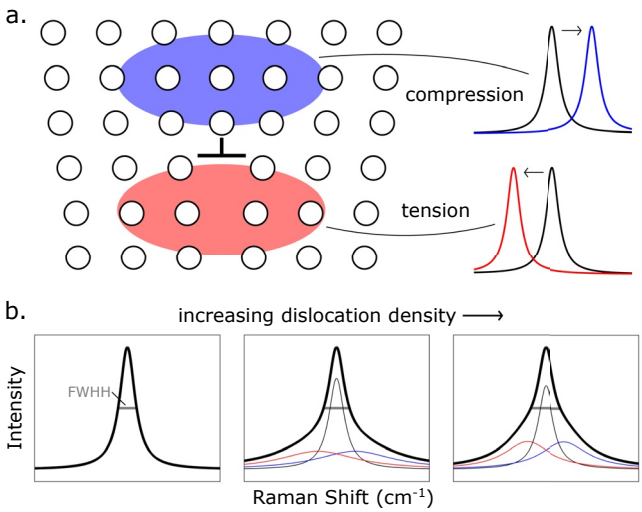

Figure 13. Simplified illustrations of how strain near a dislocation core may influence the width of peaks in Raman spectra. (a) Representation of a crystal lattice with an edge dislocation. The presence of the dislocation introduces local strain in the lattice. Compressive strain occurs above the core of the dislocation and results in a shift to higher frequencies, whereas tensile strain occurs below the edge and results in a shift to lower frequencies. (b) Representation of Raman spectra from crystals with varying dislocation densities. The presence of compressive (blue peaks) and tensile (red peaks) strain near dislocations combines with the dislocation-free regions (black lines) and results in an increase in the full width half height (FWHH) of the Raman peak (thick black line).

4.8. Quantitative Shocked Olivine Barometry by Raman Spectroscopy

The results presented in Figure 11 reveal a linear dependence of the FWHH on peak shock pressure. This relationship is compatible with the model presented in Figure 13, where the local strains introduced by the presence of dislocations result in a subset of Si-O stretching frequencies either upshifted or downshifted with respect to that of the unstrained crystal structure. The strain-induced frequency shifts are small and cannot be resolved from the unstrained olivine Raman band in the Raman spectrum. Thus, in the Raman spectrum of olivine, we observe an increase in bandwidth of the 825 and 857 cm^{-1} bands with strain. The dependence of FWHH on dislocation density has been confirmed by recent results from synchrotron-based Raman spectroscopy that reveal local variation in FWHH near the cores of edge dislocations in gallium nitride (Kokubo et al., 2018). Micro-Raman analyses of dislocations in gallium arsenide reveal a similar phenomenon: the strain field directly adjacent to a dislocation core results in frequency shifts that are manifested as an increase in the value of FWHH (Irmer & Jurisch, 2007). We do not observe the slight shift in positions for the 825 and 856 cm^{-1} olivine Raman bands that were observed in experimentally shocked olivine at higher pressure (Harriss & Burchell, 2016).

The result of the local variation in Raman band peak wavenumber in the vicinity of dislocations is manifested as broadening of the characteristic peaks with increasing dislocation density as presented in Figure 13.

The pressure-dependent shifts in the frequencies of Raman bands are well documented. In situ observations of Raman measurements in olivine revealed that frequencies of the 825 and 856 cm^{-1} bands in olivine generally increase linearly with hydrostatic confining pressure (Besson et al., 1982; Yasuzuka et al., 2009), but do not preserve this shift when returned to lower ambient pressure conditions (Farrell-Turner et al., 2005). In contrast, elastic strain has been measured at distances greater than 1 μm from the cores of dislocations (Irmer & Jurisch, 2007). These observations suggest that the coupled compressive and tensile strain around the cores of dislocations are the primary mechanisms that result in increases in the FWHH of shocked olivine that is preserved at ambient conditions.

4.9. Implications for Shocked Planetary Materials

The common occurrence of dislocation loops with b = [001] in our experimentally shocked olivine grains as well as those observed in meteorites (Ashworth & Barber, 1975; Hallis et al., 2017; Langenhorst et al., 1995; Lee et al., 2013; Madon & Poirier, 1983) suggests that similar processes of dislocation generation operate under laboratory and natural shock conditions. However, careful consideration is needed before attempting direct comparisons of the results presented above to those obtained from planetary samples. The different conditions of shock generated during FPA experiments compared to those that occur during natural impact on planetary bodies must be considered. Experiments, such as the ones presented herein, have lower entropy and shock wave duration than natural impacts. This lower entropy means that for the same peak pressures achieved, the magnitude and duration of post-shock temperature increases are significantly lower than those that would occur in a natural impact. Results from FPA experiments therefore give insight into the formation of defects directly after a shock wave has propagated through the sample and before the annealing that planetary material experience.

Sustained high-temperature conditions, such as after impact on planetary bodies, result in a reduction in dislocation density in olivine and other silicate minerals. The reduction of dislocation density occurs primarily by annihilation of dislocations of opposite sign and is aided by the rate of climb of dislocations, which is strongly dependent on temperature. The rate of dislocation annihilation is well documented for olivine based

primarily on measurements of dislocation densities before and after high-temperature annealing experiments (Farla et al., 2011; Karato & Ogawa, 1982; Kohlstedt et al., 1980; Wang et al., 2016).

Models of post-shock cooling rates of material that is ejected from planetary bodies during impact events may be used to estimate the effect of post-shock annealing on dislocation densities in meteorites. For a planetary body with a surface temperature of 0°C, a shock event with a peak pressure of 40 GPa would result in a dislocation $\sim 10^{14}$ m^{-2} for olivine crystals shocked in the $[110]_c$ orientation and an increase in temperature of ~475°C (Stöffler et al., 1991). For an annealing time of one Earth year, a reduction in dislocation density of less than 0.1% would occur for olivine based on observations of dislocation densities before and after high-temperature annealing of olivine (Farla et al., 2011).

For the condition of the most highly shocked meteorites that originated from the surface of Mars, which experienced peak shock pressures of 50 GPa and post-shock increases of 1000°C (Fritz et al., 2005), the dislocation density would be reduced by ~82% if temperature was maintained at 1000°C for one Earth year. However, ejection of meteorites into space results in rapid cooling, such that the center of a 1-m diameter piece of Martian crust would only sustain a core temperature of 1000°C for ~3 hr before quickly cooling (Fritz et al., 2005). Such a timescale that would result in a reduction in dislocation density of 0.004%. Moreover, shock features in meteorites are very localized with areas exhibiting shock melt and others showing only mild or no deformation of the original igneous texture with high temperatures (≤1200°C) sustained for short period of times (<1s) within 50 μm of a shock melt area (e.g., Sharp et al., 2019).

The rate of dislocation annihilation would only be slightly enhanced by the presence of hydrogen or higher iron content in crystals through the enhancement of the rate of climb of dislocations for these conditions and timescales. For example, using a typical Fo number of Martian olivine of 75, a decrease in viscosity of olivine of ~20 relative to Fo_{90} is predicted based on laboratory experiments of deforming via the motion of dislocations in a climb-controlled rheological regime (Tasaka et al., 2015). Assuming a 20× increase in the rate of climb and therefore annihilation of dislocations for Fo_{75} compared to Fo_{90}, a decrease in dislocation density of 0.08% for an ejected Martian meteorite that experienced a peak temperature of 1000°C for 3 hr would be expected. Therefore, increases in post-shock temperatures are unlikely to have a significant effect on dislocation densities in olivine of a range of compositions for most meteorites, which were ejected into space immediately after impact on a planetary body.

5. Conclusions

The density of GNDs varies with increasing peak shock pressure with the highest GND densities occurring at ~40 GPa. The full width at half height of Raman spectra increases linearly with peak shock pressure over all investigated shock pressures. TEM and EBSD-GND analyses reveal variable dislocation densities in shocked crystals with the highest dislocation densities occurring near fractures and grain boundaries. The types of dislocations generated during shock of olivine crystals depend on grain orientation relative to the propagation direction of the shock wave but are independent of the starting hydrogen contents of the crystals. In crystals where all of the dislocations' slip systems have low values of Schmid factor, that is, with the force vector oriented at a high angle relative to the slip plane and slip direction, the most common types of dislocations are (010)[001] edges and screws with the Burgers vector b = [001]. In contrast, for crystals oriented with high values of Schmid factor for (010)[100], that is, with a force vector at ~45° to the slip plane and slip direction, the most common types are (010)[100] and (001)[100] edge dislocations. Dislocation microstructures formed during shock experiments are remarkably similar to those observed in meteorites, suggesting similar generation processes. For dislocation recovery rates in olivine, insignificant modification of dislocation density is likely to occur due to post-shock thermal increases for meteorites ejected from planetary bodies. Finally, Raman spectroscopy is a promising technique to assess shock pressure sustained by olivine in meteorites.

Data Availability Statement

All data presented in this paper are available at the Open Science Framework data repository (Tielke, 2022).

Acknowledgments
This work would not be possible without the laboratory expertise of Roland Montes. The assistance of Frank Cardenas, Jordyn-Marie Dudley, and Christopher Snead with sample preparation is much appreciated. The manuscript was greatly improved by the thoughtful comments of Laurent Montesi and two anonymous reviewers. This work was supported by a grant from the Emerging Worlds program of NASA awarded to A. H. Peslier, solicitation #NNH16ZDA001N-EW.

References

Ashworth, J. R., & Barber, D. J. (1975). Electron petrography of shock-deformed olivine in stony meteorites. *Earth and Planetary Science Letters*, *27*(1), 43–50. https://doi.org/10.1016/0012-821x(75)90158-2

Austin, R. A., Barton, N. R., Howard, W. M., & Fried, L. E. (2014). Modeling pore collapse and chemical reactions in shock-loaded HMX crystals. *Journal of Physics: Conference Series*, *500*(Part 5), 052002. https://doi.org/10.1088/1742-6596/500/5/052002

Bachmann, F., Hielscher, R., & Schaeben, H. (2010). Texture analysis with MTEX-free and open source software toolbox. *Solid State Phenomena*, *160*, 63–68. https://doi.org/10.4028/www.scientific.net/ssp.160.63

Bai, Q., & Kohlstedt, D. L. (1992). High-temperature creep of olivine single crystals, 2. Dislocation structures. *Tectonophysics*, *206*(1–2), 1–29. https://doi.org/10.1016/0040-1951(92)90365-d

Bai, Q., Mackwell, S. J., & Kohlstedt, D. L. (1991). High-temperature creep of olivine single crystals 1. Mechanical results for buffered samples. *Journal of Geophysical Research*, *96*(B2), 2441–2463. https://doi.org/10.1029/90JB01723

Bauer, J. F. (1979). Experimental shock metamorphism of mono-and polycrystalline olivine-A comparative study. I*n Lunar and Planetary Science Conference Proceedings* (Vol. 10, pp. 2573–2596).

Bell, D. R., Rossman, G. R., Maldener, J., Endisch, D., & Rauch, F. (2003). Hydroxide in olivine: A quantitative determination of the absolute amount and calibration of the IR spectrum. *Journal of Geophysical Research*, *108*(B2), 2105. https://doi.org/10.1029/2001jb000679

Berg, S. J. (1974). Geological Society of America Bulletin. *The Geological Society of America Bulletin*, *104*(5), 528–542. https://doi.org/10.1130/0016-7606(1954)65

Besson, J. M., Pinceaux, J. P., Anastopoulos, C., & Velde, B. (1982). Raman spectra of olivine up to 65 kilobars. *Journal of Geophysical Research*, *87*(B13), 10773–10775. https://doi.org/10.1029/jb087ib13p10773

Binns, R. A. (1970). $(Mg, Fe)_2SiO_4$ spinel in a meteorite. *Physics of the Earth and Planetary Interiors*, *3*, 156–160. https://doi.org/10.1016/0031-9201(70)90048-8

Bouilhol, P., Burg, J.-P., Bodinier, J.-L., Schmidt, M. W., Bernasconi, S. M., & Dawood, H. (2012). Gem olivine and calcite mineralization precipitated from subduction-derived fluids in the Kohistan arc-mantle (Pakistan). *The Canadian Mineralogist*, *50*(5), 1291–1304. https://doi.org/10.3749/canmin.50.5.1291

Brearley, A. J., Jones, R. H., & Papike, J. J. (1998). Chondritic meteorites. In Planetary materials (p. C1).

Carter, N. L., & Ave'Lallemant, H. G. (1970). High temperature flow of dunite and peridotite. *Bulletin of the Geological Society of America*, *81*(8), 2181–2202. https://doi.org/10.1130/0016-7606(1970)81[2181:htfoda]2.0.co;2

Carter, N. L., Raleigh, C. B., & DeCarli, P. S. (1968). Deformation of olivine in stony meteorites. *Journal of Geophysical Research*, *73*(16), 5439–5461. https://doi.org/10.1029/jb073i016p05439

Cavosie, A. J., Timms, N. E., Ferrière, L., & Rochette, P. (2018). FRIGN zircon—The only terrestrial mineral diagnostic of high-pressure and high-temperature shock deformation. *Geology*, *46*(10), 891–894. https://doi.org/10.1130/g45079.1

Chao, E. C. T., Shoemaker, E. M., & Madsen, B. M. (1960). First natural occurrence of coesite. *Science*, *132*(3421), 220–222. https://doi.org/10.1126/science.132.3421.220

Chopra, P. N., & Paterson, M. S. (1984). The role of water in the derformation of dunite. *Journal of Geophysical Research*, *89*(B9), 7861–7876. https://doi.org/10.1029/JB089iB09p07861

Demouchy, S., Schneider, S. E., Mackwell, S. J., Zimmerman, M. E., & Kohlstedt, D. L. (2009). Experimental deformation of olivine single crystals at lithospheric temperatures. *Geophysical Research Letters*, *36*(4), L04304. https://doi.org/10.1029/2008gl036611

Demouchy, S., Tommasi, A., Ballaran, T. B., Cordier, P., Boffa Ballaran, T., Cordier, P., et al. (2013). Low strength of Earth's uppermost mantle inferred from tri-axial deformation experiments on dry olivine crystals. *Physics of the Earth and Planetary Interiors*, *220*, 37–49. https://doi.org/10.1016/j.pepi.2013.04.008

Dixon, N. A., & Durham, W. B. (2018). Measurement of activation volume for creep of dry olivine at upper-mantle conditions. *Journal of Geophysical Research: Solid Earth*, *123*(10), 8459–8473. https://doi.org/10.1029/2018jb015853

Durham, W. B., & Goetze, C. (1977). Plastic flow of oriented single crystals of olivine: 1. Mechanical data. *Journal of Geophysical Research*, *82*(36), 5737–5753. https://doi.org/10.1029/jb082i036p05737

Duvall, G. E., & Fowles, G. R. (1963). *High pressure physics and chemistry* (pp. 209–223). Academic Press.

Erickson, T. M., Cavosie, A. J., Pearce, M. A., Timms, N. E., & Reddy, S. M. (2016). Empirical constraints on shock features in monazite using shocked zircon inclusions. *Geology*, *44*(8), 635–638. https://doi.org/10.1130/g37979.1

Erickson, T. M., Pearce, M. A., Reddy, S. M., Timms, N. E., Cavosie, A. J., Bourdet, J., et al. (2017). Microstructural constraints on the mechanisms of the transformation to reidite in naturally shocked zircon. *Contributions to Mineralogy and Petrology*, *172*(1), 6. https://doi.org/10.1007/s00410-016-1322-0

Evans, B., & Goetze, C. (1979). The temperature variation of hardness of olivine and its implication for polycrystalline yield stress. *Journal of Geophysical Research*, *84*(B10), 5505–5524. https://doi.org/10.1029/JB084iB10p05505

Farla, R. J. M., Kokkonen, H., Gerald, J. D. F., Barnhoorn, A., Faul, U. H., & Jackson, I. (2011). Dislocation recovery in fine-grained polycrystalline olivine. *Physics and Chemistry of Minerals*, *38*(5), 363–377. https://doi.org/10.1007/s00269-010-0410-3

Farrell-Turner, S., Reimold, W. U., Nieuwoudt, M., & Erasmus, R. M. (2005). Raman spectroscopy of olivine in dunite experimentally shocked to pressures between 5 and 59 GPa. *Meteoritics & Planetary Sciences*, *40*(9–10), 1311–1327. https://doi.org/10.1111/j.1945-5100.2005.tb00403.x

Frank, F. C., & Read, W. T., Jr. (1950). Multiplication processes for slow moving dislocations. *Physical Review*, *79*(4), 722–723. https://doi.org/10.1103/physrev.79.722

Fritz, J., Artemieva, N., & Greshake, A. (2005). Ejection of Martian meteorites. *Meteoritics & Planetary Sciences*, *40*(9–10), 1393–1411. https://doi.org/10.1111/j.1945-5100.2005.tb00409.x

Fritz, J., Assis Fernandes, V., Greshake, A., Holzwarth, A., & Böttger, U. (2019). On the formation of diaplectic glass: Shock and thermal experiments with plagioclase of different chemical compositions. *Meteoritics & Planetary Sciences*, *54*(7), 1533–1547. https://doi.org/10.1111/maps.13289

Fritz, J., Greshake, A., & Fernandes, V. A. (2017). Revising the shock classification of meteorites. *Meteoritics & Planetary Sciences*, *52*(6), 1216–1232. https://doi.org/10.1111/maps.12845

Gault, D. E. (1963). The partition of energy for hypervelocity impact craters formed in rock. *Proceedings of the Sixth Hypervelocity Impact Symposium*, *2*, 419–456.

Gibbons, R. V. (1974). *Experimental effects of high shock pressure on materials of geological and geophysical interest*. California Institute of Technology.

Gibbons, R. V., & Ahrens, T. J. (1971). Shock metamorphism of silicate glasses. *Journal of Geophysical Research*, *76*(23), 5489–5498. https://doi.org/10.1029/jb076i023p05489

Gibbons, R. V., & Ahrens, T. J. (1977). Effects of shock pressures on calcic plagioclase. *Physics and Chemistry of Minerals*, *1*(1), 95–107. https://doi.org/10.1007/bf00307982

Glass, B. P., & Fries, M. (2008). Micro-Raman spectroscopic study of fine-grained, shock-metamorphosed rock fragments from the Australasian microtektite layer. *Meteoritics & Planetary Sciences*, *43*(9), 1487–1496. https://doi.org/10.1111/j.1945-5100.2008.tb01023.x

Goltrant, O., Cordier, P., & Doukhan, J.-C. (1991). Planar deformation features in shocked quartz; a transmission electron microscopy investigation. *Earth and Planetary Science Letters*, *106*(1–4), 103–115. https://doi.org/10.1016/0012-821x(91)90066-q

Greshake, A., Fritz, J., Böttger, U., & Goran, D. (2013). Shear-induced ringwoodite formation in the Martian shergottite Dar al Gani 670. *Earth and Planetary Science Letters*, *375*, 383–394. https://doi.org/10.1016/j.epsl.2013.06.002

Greshake, A., Fritz, J., & Stöffler, D. (2004). Petrology and shock metamorphism of the olivine-phyric shergottite Yamato 980459: Evidence for a two-stage cooling and a single-stage ejection history. *Geochimica et Cosmochimica Acta*, *68*(10), 2359–2377. https://doi.org/10.1016/j.gca.2003.11.022

Hallis, L. J., Huss, G. R., Nagashima, K., Taylor, G. J., Stöffler, D., Smith, C. L., & Lee, M. R. (2017). Effects of shock and Martian alteration on Tissint hydrogen isotope ratios and water content. *Geochimica et Cosmochimica Acta*, *200*, 280–294. https://doi.org/10.1016/j.gca.2016.12.035

Hansen, L. N., Kumamoto, K. M., Thom, C. A., Wallis, D., Durham, W. B., Goldsby, D. L., et al. (2019). Low-temperature plasticity in olivine: Grain size, strain hardening, and the strength of the lithosphere. *Journal of Geophysical Research: Solid Earth*, *124*(6), 5427–5449. https://doi.org/10.1029/2018jb016736

Harriss, K. H., & Burchell, M. J. (2016). A study of the observed shift in the peak position of olivine Raman spectra as a result of shock induced by hypervelocity impacts. *Meteoritics & Planetary Sciences*, *51*(7), 1289–1300. https://doi.org/10.1111/maps.12660

Hielscher, R., Silbermann, C. B., Schmidl, E., & Ihlemann, J. (2019). *Denoising of crystal orientation maps* (pp. 984–996).

Hirth, G., & Kohlstedt, D. L. (2015). The stress dependence of olivine creep rate: Implications for extrapolation of lab data and interpretation of recrystallized grain size. *Earth and Planetary Science Letters*, *418*, 20–26. https://doi.org/10.1016/j.epsl.2015.02.013

Hornbogen, E. (1962). The role of strain energy during precipitation of copper and gold from alpha iron. *Acta Metallurgica*, *10*(5), 525–533. https://doi.org/10.1016/0001-6160(62)90197-9

Hörz, F. (1970). *A small ballistic range for impact metamorphism studies* (Vol. 5787). National Aeronautics and Space Administration.

Hu, J., & Sharp, T. G. (2017). Back-transformation of high-pressure minerals in shocked chondrites: Low-pressure mineral evidence for strong shock. *Geochimica et Cosmochimica Acta*, *215*, 277–294. https://doi.org/10.1016/j.gca.2017.07.018

Idrissi, H., Bollinger, C., Boioli, F., Schryvers, D., & Cordier, P. (2016). Low-temperature plasticity of olivine revisited with in situ TEM nanomechanical testing. *Science Advances*, *2*(3), e1501671. https://doi.org/10.1126/sciadv.1501671

Irmer, G., & Jurisch, M. (2007). Micro-Raman study of strain fields around dislocations in GaAs. *Physica Status Solidi*, *204*(7). https://doi.org/10.1002/pssa.200623041

Jacobsen, S. D., Jiang, F., Mao, Z., Duffy, T. S., Smyth, J. R., Holl, C. M., & Frost, D. J. (2008). Effects of hydration on the elastic properties of olivine. *Geophysical Research Letters*, *35*(14), L14303. https://doi.org/10.1029/2008gl034398

Jakubek, R. S., & Fries, M. D. (2020). Calibration of Raman wavenumber in large Raman images using a mercury-argon lamp. *Journal of Raman Spectroscopy*, *51*(7), 1172–1185. https://doi.org/10.1002/jrs.5887

Jakubek, R. S., & Fries, M. D. (2021). Calibration of Raman bandwidth in large Raman images using a mercury–argon lamp. *Journal of Raman Spectroscopy*, *52*(3), 709–722. https://doi.org/10.1002/jrs.6045

Jaret, S. J., Woerner, W. R., Phillips, B. L., Ehm, L., Nekvasil, H., Wright, S. P., & Glotch, T. D. (2015). Maskelynite formation via solid-state transformation: Evidence of infrared and X-ray anisotropy. *Journal of Geophysical Research: Planets*, *120*(3), 570–587. https://doi.org/10.1002/2014je004764

Jenkins, L. E., Flemming, R. L., & McCausland, P. J. A. (2019). Quantitative in situ XRD measurement of shock metamorphism in Martian meteorites using lattice strain and strain-related mosaicity in olivine. *Meteoritics & Planetary Sciences*, *54*(4), 902–918. https://doi.org/10.1111/maps.13245

Jiang, J., Britton, T. B., & Wilkinson, A. J. (2013). Measurement of geometrically necessary dislocation density with high resolution electron backscatter diffraction: Effects of detector binning and step size. *Ultramicroscopy*, *125*, 1–9. https://doi.org/10.1016/j.ultramic.2012.11.003

Karato, S.-I. (2012). *Deformation of earth materials: An introduction to the rheology of solid earth*. Cambridge University Press.

Karato, S. I., & Jung, H. (2003). Effects of pressure on high-temperature dislocation creep in olivine. *Philosophical Magazine*, *83*(3), 401–414. https://doi.org/10.1080/0141861021000025829

Karato, S.-I., & Ogawa, M. (1982). High-pressure recovery of olivine: Implications for creep mechanisms and creep activation volume. *Physics of the Earth and Planetary Interiors*, *28*(2), 102–117. https://doi.org/10.1016/0031-9201(82)90076-0

Keefner, J. W., Mackwell, S. J., Kohlstedt, D. L., & Heidelbach, F. (2011). Dependence of dislocation creep of dunite on oxygen fugacity: Implications for viscosity variations in Earth's mantle. *Journal of Geophysical Research*, *116*(B5), B05201. https://doi.org/10.1029/2010jb007748

Kieffer, S. W. (1971). Shock metamorphism of the Coconino sandstone at Meteor Crater, Arizona. *Journal of Geophysical Research*, *76*(23), 5449–5473. https://doi.org/10.1029/jb076i023p05449

Kieffer, S. W. (1975). From regolith to rock by shock. *The Moon*, *13*(1–3), 301–320. https://doi.org/10.1007/bf00567522

Kohlstedt, D. L., Goetze, C., Durham, W. B., & Vander Sande, J. (1976). New technique for decorating dislocations in olivine. *Science*, *191*(4231), 1045–1046. https://doi.org/10.1126/science.191.4231.1045

Kohlstedt, D. L., Nichols, H. P. K., & Hornack, P. (1980). The effect of pressure on the rate of dislocation recovery in olivine. *Journal of Geophysical Research*, *85*(B6), 3122–3130. https://doi.org/10.1029/jb085ib06p03122

Kokubo, N., Tsunooka, Y., Fujie, F., Ohara, J., Hara, K., Onda, S., et al. (2018). Detection of edge component of threading dislocations in GaN by Raman spectroscopy. *Applied Physics Express*, *11*(6), 61002. https://doi.org/10.7567/apex.11.061002

Kubin, L. P., & Mortensen, A. (2003). Geometrically necessary dislocations and strain-gradient plasticity: A few critical issues. *Scripta Materialia*, *48*(2), 119–125. https://doi.org/10.1016/s1359-6462(02)00335-4

Langenhorst, F., Boustie, M., Migault, A., & Romain, J. P. (1999). Laser shock experiments with nanoseconds pulses: A new tool for the reproduction of shock defects in olivine. *Earth and Planetary Science Letters*, *173*(3), 333–342. https://doi.org/10.1016/s0012-821x(99)00224-1

Langenhorst, F., Joreau, P., & Doukhan, J. C. (1995). Thermal and shock metamorphism of the Tenham chondrite: A TEM examination. *Geochimica et Cosmochimica Acta*, *59*(9), 1835–1845. https://doi.org/10.1016/0016-7037(95)00086-f

Langenhorst, F., Poirier, J. P., Deutsch, A., & Hornemann, U. (2002). Experimental approach to generate shock veins in single crystal olivine by shear melting. *Meteoritics & Planetary Sciences*, *37*(11), 1541–1553. https://doi.org/10.1111/j.1945-5100.2002.tb00809.x

Lee, M. R., Tomkinson, T., Mark, D. F., Stuart, F. M., & Smith, C. L. (2013). Evidence for silicate dissolution on Mars from the Nakhla meteorite. *Meteoritics & Planetary Sciences*, *48*(2), 224–240. https://doi.org/10.1111/maps.12053

Leroux, H. (2001). Microstructural shock signatures of major minerals in meteorites. *European Journal of Mineralogy*, *13*(2), 253–272. https://doi.org/10.1127/0935-1221/01/0013-0253

Leroux, H., Doukhan, J. C., & Langenhorst, F. (1994). Microstructural defects in experimentally shocked diopside: A TEM characterization. *Physics and Chemistry of Minerals*, *20*(8), 521–530. https://doi.org/10.1007/bf00211847

Libowitzky, E., & Beran, A. (2006). The structure of hydrous species in nominally anhydrous minerals: Information from polarized IR spectroscopy. *Reviews in Mineralogy and Geochemistry*, *62*(1), 29–52. https://doi.org/10.2138/rmg.2006.62.2

Mackwell, S. J., Kohlstedt, D. L., & Paterson, M. S. (1985). The role of water in the deformation of olivine single crystals. *Journal of Geophysical Research*, *90*(B13), 11311–11319. https://doi.org/10.1029/jb090ib13p11319

Madon, M., & Poirier, J. P. (1983). Transmission electron microscope observation of α, β and γ (Mg, Fe)$_2$SiO$_4$ in shocked meteorites: Planar defects and polymorphic transitions. *Physics of the Earth and Planetary Interiors*, *33*(1), 31–44. https://doi.org/10.1016/0031-9201(83)90005-5

Malavergne, V., Guyot, F., Benzerara, K., & Martinez, I. (2001). Description of new shock-induced phases in the Shergotty, Zagami, Nakhla and Chassigny meteorites. *Meteoritics & Planetary Sciences*, *36*(10), 1297–1305. https://doi.org/10.1111/j.1945-5100.2001.tb01825.x

McSween, H. Y., Jr. (2015). Petrology on Mars. *American Mineralogist*, *100*(11–12), 2380–2395. https://doi.org/10.2138/am-2015-5257

Mei, S., & Kohlstedt, D. L. (2000). Influence of water on plastic deformation of olivine aggregates: 2. Dislocation creep regime. *Journal of Geophysical Research*, *105*(B9), 21471–21481. https://doi.org/10.1029/2000JB900180

Mei, S., Suzuki, A. M., Kohlstedt, D. L., Dixon, N. A., & Durham, W. B. (2010). Experimental constraints on the strength of the lithospheric mantle. *Journal of Geophysical Research*, *115*(B0), B08204. https://doi.org/10.1029/2009JB006873

Meyers, M. A. (1978). A mechanism for dislocation generation in shock-wave deformation. *Scripta Metallurgica*, *12*(1), 21–26. https://doi.org/10.1016/0036-9748(78)90219-3

Meyers, M. A., Jarmakani, H., Bringa, E. M., & Remington, B. A. (2009). Dislocations in shock compression and release. *Dislocations in Solids*, *15*, 91–197.

Miller, G. H., Rossman, G. R., & Harlow, G. E. (1987). The natural occurrence of hydroxide in olivine. *Physics and Chemistry of Minerals*, *14*(5), 461–472. https://doi.org/10.1007/bf00628824

Mittlefehldt, D. W., McCoy, T. J., Goodrich, C. A., & Kracher, A. (2018). Non-chondritic meteorites from asteroidal bodies. In *Planetary materials* (pp. 523–718). De Gruyter.

Miyamoto, M., & Ohsumi, K. (1995). Micro Raman spectroscopy of olivines in L6 chondrites: Evaluation of the degree of shock. *Geophysical Research Letters*, *22*(4), 437–440. https://doi.org/10.1029/94gl03281

Mouri, T., & Enami, M. (2008). Raman spectroscopic study of olivine-group minerals. *Journal of Mineralogical and Petrological Sciences*, *103*(2), 100–104. https://doi.org/10.2465/jmps.071015

Ohtani, E., & Kumazawa, M. (1981). Melting of forsterite Mg2SiO4 up to 15 GPa. *Physics of the Earth and Planetary Interiors*, *27*(1), 32–38. https://doi.org/10.1016/0031-9201(81)90084-4

Orowan, E. (1940). Problems of plastic gliding. *Proceedings of the Physical Society*, *52*(1), 8–22. https://doi.org/10.1088/0959-5309/52/1/303

Paterson, M. S. (1982). The determination of hydroxyl by infrared absorption in quartz, silicate glasses and similar materials. *Bulletin de Mineralogie*, *105*(1), 20–29. https://doi.org/10.3406/bulmi.1982.7582

Peach, M., & Koehler, J. S. (1950). The forces exerted on dislocations and the stress fields produced by them. *Physical Review*, *80*(3), 436–439. https://doi.org/10.1103/physrev.80.436

Peslier, A. H., Hnatyshin, D., Herd, C. D. K., Walton, E. L., Brandon, A. D., Lapen, T. J., & Shafer, J. T. (2010). Crystallization, melt inclusion, and redox history of a Martian meteorite: Olivine-phyric shergottite Larkman Nunatak 06319. *Geochimica et Cosmochimica Acta*, *74*(15), 4543–4576. https://doi.org/10.1016/j.gca.2010.05.002

Piazolo, S., La Fontaine, A., Trimby, P., Harley, S., Yang, L., Armstrong, R., & Cairney, J. M. (2016). Deformation-induced trace element redistribution in zircon revealed using atom probe tomography. *Nature Communications*, *7*, 1–7. https://doi.org/10.1038/ncomms10490

Pouchou, J. L., & Pichoir, F. (1984). A new model for quantitative x-ray microanalysis. I. Application to the analysis of homogeneous samples. *Recherche Aerospatiale*, (3), 167–192.

Raterron, P., Chen, J., Geenen, T., & Girard, J. (2011). Pressure effect on forsterite dislocation slip systems: Implications for upper-mantle LPO and low viscosity zone. *Physics of the Earth and Planetary Interiors*, *188*(1), 26–36. https://doi.org/10.1016/j.pepi.2011.06.009

Reimold, W. U., & Stöffler, D. (1978). Experimental shock metamorphism of dunite. In *Lunar and Planetary Science Conference Proceedings* (Vol. 9, pp. 2805–2824).

Rhodes, J. M., & Hubbard, N. J. (1973). Chemistry, classification, and petrogenesis of Apollo 15 mare basalts. In *Lunar and Planetary Science Conference Proceedings* (Vol. 4, p. 1127).

Rubin, A. E. (2015). Maskelynite in asteroidal, lunar and planetary basaltic meteorites: An indicator of shock pressure during impact ejection from their parent bodies. *Icarus*, *257*, 221–229. https://doi.org/10.1016/j.icarus.2015.05.010

Schaal, R. B., & Horz, F. (1980). Experimental shock metamorphism of lunar soil. *Lunar and Planetary Science Conference Proceedings*, *11*, 1679–1695.

Schaal, R. B., Hörz, F., Thompson, T. D., & Bauer, J. F. (1979). Shock metamorphism of granulated lunar basalt. *Lunar and Planetary Science Conference Proceedings*, *10*, 2547–2571.

Schmid, E., & Boas, W. (1935). *Kristallplastizität mit besonderer Berücksichtigung der Metalle*. In *Springer-Verlag Berlin Heidelberg GmbH* (Vol. 17). Springer-Verlag. https://doi.org/10.1017/CBO9781107415324.004

Sharp, T. G., & DeCarli, P. S. (2006). Shock effects in meteorites. *Meteorites and the Early Solar System II*, *943*, 653–677.

Sharp, T. G., Walton, E. L., Hu, J., & Agee, C. (2019). Shock conditions recorded in NWA 8159 Martian augite basalt with implications for the impact cratering history on Mars. *Geochimica et Cosmochimica Acta*, *246*, 197–212. https://doi.org/10.1016/j.gca.2018.11.014

Shehadeh, M. A., & Zbib, H. M. (2016). On the homogeneous nucleation and propagation of dislocations under shock compression. *Philosophical Magazine*, *96*(26), 2752–2778. https://doi.org/10.1080/14786435.2016.1213444

Shen, P., Hwang, S.-L., Chu, H.-T., & Yui, T.-F. (2001). α-PbO$_2$–Type TiO$_2$: From Mineral physics to natural occurrence. *International Geology Review*, *43*(4), 366–378. https://doi.org/10.1080/00206810109465018

Shinno, I., Nakamuta, Y., Nakamura, T., & Sekine, T. (1999). Characterization of artificially shocked forsterites: (2) Profile analysis of photo-luminescence spectra. *Mineralogical Journal*, *21*(3), 119–130. https://doi.org/10.2465/minerj.21.119

Sichani, M. M., & Spearot, D. E. (2016). A molecular dynamics study of dislocation density generation and plastic relaxation during shock of single crystal Cu. *Journal of Applied Physics*, *120*(4), 045902. https://doi.org/10.1063/1.4959075

Smith, C. S. (1958). Metallographic studies of metals after explosive shock. *Transactions of the Metallurgical Society of AIME*, *212*.

Stöffler, D., Hamann, C., & Metzler, K. (2018). Shock metamorphism of planetary silicate rocks and sediments: Proposal for an updated classification system. *Meteoritics & Planetary Sciences*, *53*(1), 5–49. https://doi.org/10.1111/maps.12912

Stöffler, D., Keil, K., & Edward, R. D. S. (1991). Shock metamorphism of ordinary chondrites. *Geochimica et Cosmochimica Acta*, *55*(12), 3845–3867. https://doi.org/10.1016/0016-7037(91)90078-J

Takenouchi, A., Mikouchi, T., Kobayashi, T., Sekine, T., Yamaguchi, A., & Ono, H. (2019). Fine-structures of planar deformation features in shocked olivine: A comparison between Martian meteorites and experimentally shocked basalts as an indicator for shock pressure. *Meteoritics & Planetary Sciences*, *54*(9), 1990–2005. https://doi.org/10.1111/maps.13367

Tasaka, M., Zimmerman, M. E., & Kohlstedt, D. L. (2015). Creep behavior of Fe-bearing olivine under hydrous conditions. *Journal of Geophysical Research: Solid Earth*, *120*(9), 6039–6057. https://doi.org/10.1002/2015jb012096

Tielke, J. (2022). Data from experimentally impacted olivine crystals. *Open Science Framework*. https://doi.org/10.17605/OSF.IO/RXZ83

Tielke, J., Mecklenburgh, J., Mariani, E., & Wheeler, J. (2019). The influence of water on the strength of olivine dislocation slip systems. *Journal of Geophysical Research: Solid Earth*, *124*(7), 6542–6559. https://doi.org/10.1029/2019JB017436

Tielke, J. A., Zimmerman, M. E., & Kohlstedt, D. L. (2016). Direct shear of olivine single crystals. *Earth and Planetary Science Letters*, *455*(001), 140–148. https://doi.org/10.1016/j.epsl.2016.09.002

Tielke, J. A., Zimmerman, M. E., & Kohlstedt, D. L. (2017). Hydrolytic weakening in olivine single crystals. *Journal of Geophysical Research: Solid Earth*, *122*(5), 3465–3479. https://doi.org/10.1002/2017JB014004

Tomioka, N., & Miyahara, M. (2017). High-pressure minerals in shocked meteorites. *Meteoritics & Planetary Sciences*, *52*(9), 2017–2039. https://doi.org/10.1111/maps.12902

Tschauner, O., Ma, C., Lanzirotti, A., & Newville, M. G. (2020). Riesite, a new high pressure polymorph of TiO_2 from the Ries impact structure. *Minerals*, *10*(1), 78. https://doi.org/10.3390/min10010078

Uchizono, A., Shinno, I., Nakamuta, Y., Nakamura, T., & Sekine, T. (1999). Characterization of artificially shocked forsterites: (1) Diffraction profile analysis by Gandolfi Camera. *Mineralogical Journal*, *21*(1), 15–23. https://doi.org/10.2465/minerj.21.15

Udry, A., Howarth, G. H., Herd, C. D. K., Day, J. M. D., Lapen, T. J., & Filiberto, J. (2020). *What Martian meteorites reveal about the interior and surface of Mars*. Wiley Online Library.

Wallis, D., Hansen, L. N., Ben Britton, T., & Wilkinson, A. J. (2016). Geometrically necessary dislocation densities in olivine obtained using high-angular resolution electron backscatter diffraction. *Ultramicroscopy*, *168*, 34–45. https://doi.org/10.1016/j.ultramic.2016.06.002

Wallis, D., Hansen, L. N., Tasaka, M., Kumamoto, K. M., Parsons, A. J., Lloyd, G. E., et al. (2019). The impact of water on slip system activity in olivine and the formation of bimodal crystallographic preferred orientations. *Earth and Planetary Science Letters*, *508*, 51–61. https://doi.org/10.1016/j.epsl.2018.12.007

Walton, E. L., & Herd, C. D. K. (2007). Localized shock melting in lherzolitic shergottite Northwest Africa 1950: Comparison with Allan Hills 77005. *Meteoritics & Planetary Sciences*, *42*(1), 63–80. https://doi.org/10.1111/j.1945-5100.2007.tb00218.x

Walton, E. L., & Shaw, C. S. J. (2009). Understanding the textures and origin of shock melt pockets in Martian meteorites from petrographic studies, comparisons with terrestrial mantle xenoliths, and experimental studies. *Meteoritics & Planetary Sciences*, *44*(1), 55–76. https://doi.org/10.1111/j.1945-5100.2009.tb00717.x

Wang, L., Blaha, S., Pintér, Z., Farla, R., Kawazoe, T., Miyajima, N., et al. (2016). Temperature dependence of [100](010) and [001](010) dislocation mobility in natural olivine. *Earth and Planetary Science Letters*, *441*, 81–90. https://doi.org/10.1016/j.epsl.2016.02.029

Wheeler, J., Mariani, E., Piazolo, S., Prior, D. J., Trimby, P., & Drury, M. R. (2009). The weighted Burgers vector: A new quantity for constraining dislocation densities and types using electron backscatter diffraction on 2D sections through crystalline materials. *Journal of Microscopy*, *233*(3), 482–494. https://doi.org/10.1111/j.1365-2818.2009.03136.x

Wilkinson, A. J. (2001). A new method for determining small misorientations from EBSD patterns. *Scripta Materialia*, *44*(10), 2379–2385. https://doi.org/10.1016/s1359-6462(01)00943-5

Xie, X., Minitti, M. E., Chen, M., Mao, H.-K., Wang, D., Shu, J., & Fei, Y. (2002). Natural high-pressure polymorph of merrillite in the shock veins of the Suizhou meteorite. *Geochimica et Cosmochimica Acta*, *66*(13), 2439–2444. https://doi.org/10.1016/s0016-7037(02)00833-5

Xie, Z., Sharp, T. G., & De Carli, P. S. (2006). Estimating shock pressures based on high-pressure minerals in shock-induced melt veins of L chondrites. *Meteoritics & Planetary Sciences*, *41*(12), 1883–1898. https://doi.org/10.1111/j.1945-5100.2006.tb00458.x

Yasuzuka, T., Ishibashi, H., Arakawa, M., Yamamoto, J., & Kagi, H. (2009). Simultaneous determination of Mg# and residual pressure in olivine using micro-Raman spectroscopy. *Journal of Mineralogical and Petrological Sciences*, *104*(6), 911280114. https://doi.org/10.2465/jmps.090615

Zaretsky, E. (1995). Dislocation multiplication behind the shock front. *Journal of Applied Physics*, *78*(6), 3740–3747. https://doi.org/10.1063/1.359954

References From the Supporting Information

Asthana, B. P., & Kiefer, W. (1982). Deconvolution of the Lorentzian Linewidth and determination of fraction Lorentzian Character from the observed profile of a Raman line by a Comparison Technique. *Applied Spectroscopy*, *36*(3), 250–257. https://doi.org/10.1366/0003702824638647

Bai, Q., Mackwell, S. J., & Kohlstedt, D. L. (1991). High-temperature creep of olivine single crystals 1. Mechanical results for buffered samples. *Journal of Geophysical Research*, *96*(B2), 2441–2463. https://doi.org/10.1029/90JB01723

Farla, R. J. M., Kokkonen, H., Gerald, J. D. F., Barnhoorn, A., Faul, U. H., & Jackson, I. (2011). Dislocation recovery in fine-grained polycrystalline olivine. *Physics and Chemistry of Minerals*, *38*(5), 363–377. https://doi.org/10.1007/s00269-010-0410-3

Hielscher, R., Silbermann, C. B., Schmidl, E., & Ihlemann, J. (2019). *Denoising of crystal orientation maps* (pp. 984–996).

Jakubek, R. S., & Fries, M. D. (2021). Calibration of Raman bandwidth in large Raman images using a mercury–argon lamp. *Journal of Raman Spectroscopy*, *52*(3), 709–722. https://doi.org/10.1002/jrs.6045

Jung, H., & Karato, S.-I. (2001). Effects of water on dynamically recrystallized grain size of olivine. *Journal of Structural Geology*, *23*(9), 1337–1344. https://doi.org/10.1016/S0191-8141(01)00005-0

Karato, S. I., Paterson, M. S., & FitzGerald, J. D. (1986). Rheology of synthetic olivine aggregates: Influence of grain size and water. *Journal of Geophysical Research: Solid Earth*, *91*(B8), 8151–8176.

Kohlstedt, D. L., Goetze, C., Durham, W. B., & Vander Sande, J. (1976). New technique for decorating dislocations in olivine. *Science*, *191*(4231), 1045–1046. https://doi.org/10.1126/science.191.4231.1045

Ohuchi, T., Karato, S. I., & Fujino, K. (2011). Strength of single-crystal orthopyroxene under lithospheric conditions. *Contributions to Mineralogy and Petrology*, *161*(6), 961–975. https://doi.org/10.1007/s00410-010-0574-3

Tielke, J. A., Zimmerman, M. E., & Kohlstedt, D. L. (2017). Hydrolytic weakening in olivine single crystals. *Journal of Geophysical Research: Solid Earth*, *122*(5), 3465–3479. https://doi.org/10.1002/2017JB014004